Seismic hazard assessment for Kalpasar dam

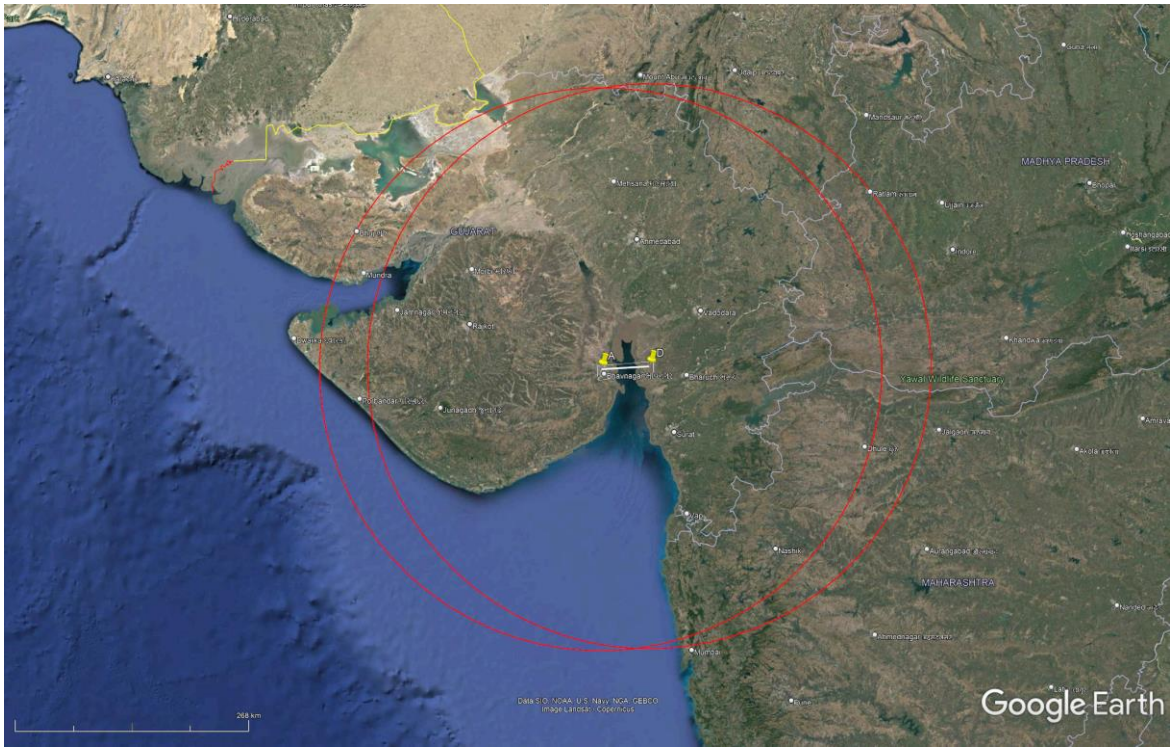

Report by

CSIR-National Geophysical Research Institute, Hyderabad

Sponsored by

National Center for Coastal Research (Ministry of Earth Sciences), Chennai

January 2022

Contents

Summary

Geology, seismicity and seismotectonics of the source regions within 300 km of the Kalpasar dam have been analysed with the view to objectively assess the seismic hazard in the Kalpasar dam region. A critical assessment of crustal deformation using GNSS measurements and InSAR analysis is made to suggest that the region around the Kalpasar dam exhibit very low strain (~1 nanostrain/year). The six identified source regions were characterized and an objective assessment of M_{max} is made for each source region. It is found that the Kachchh region, although the farthest among the six regions, has a potential to generate major earthquake in future.

Using the available geotechnical data and ground motion attenuation relations, Seismic Hazard Analysis using the DSHA and PSHA approach is done and following conclusions are drawn:

- The target spectrum for one of the locations at the eastern end (PS4) of the dam is shown in the below figure. As per the NCSDP guidelines, this target envelope spectrum was developed using the envelope of PSHA and DSHA spectra. Hence, this envelope spectrum should be used in the design of the eastern end of the dam site.

- Seismic hazard assessment at the Kalpasar dam suggests horizontal peak ground acceleration (PGA) of 0.26 – 0.23 g from western end to the eastern end of the dam. This is in keeping with international literature, which suggests that when an intensity of earthquake ground shaking is VIII on the MSK Scale, the likely PGA is in the range 0.25g–0.30g.

  Considering the above, a design PGA value of 0.26g is recommended at the dam site.

- Site-specific design accelerograms and response spectra for different damping values of the horizontal and vertical ground motions for MCE and DBE conditions have been obtained for all the four specified locations of the site.

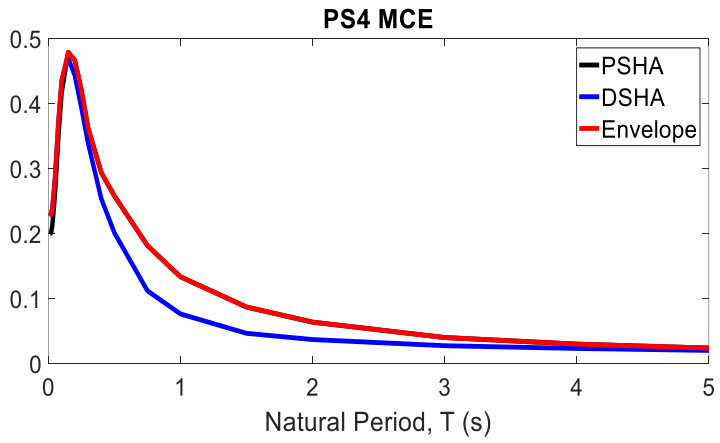

1.

Seismicity, seismotectonics, data collection and initial review

1.1 INTRODUCTION

All the information on the seismicity using various available earthquake catalogue, focal mechanism, available lineament/fault map, geology of the region, crustal deformation using GPS measurements and InSAR was collected for the seismic hazard assessment of Kalpasar dam. This information is necessary to take up further study on DSHA and PSHA. Here in this chapter, all these aspects are covered. Based on theses, input parameters will be decided for the computation of seismic hazard.

The region within 300 km around the proposed Kalpasar dam is the main focus in this study. The eastern and western abutment of the dam are at 72°38′51.17″E, 21°48′25.71″N and 72°9′2.02″E, 21°48′25.22″N, respectively.

1.2 GEOLOGY AND TECTONICS AND EARTHQUAKES OF THE REGION AROUND THE PROPOSED KALPASAR DAM

Geology of the region around the dam is dominated by the Deccan traps and failed rifts and basins, namely, Kachchh and Narmada Son region and Delhi Aravalli fold belt (**Figures 1.1** and **1.2**).

The ~300-km-long east-west trending Kachchh paleorift, which lies to the northeast of the proposed Kalpasar dam, initiated during the late Triassic breakup of the Gondwanaland by the reactivation of primordial faults in the Precambrian Delhi fold belt. The rifting was aborted during the late Cretaceous precollision stage of the Indian plate, which was followed by the sediment deposition during Mesozoic, Tertiary, and Quaternary periods (Biswas, 1987, 2005; Biswas & Khattri, 2002; Roy, 2004). On its northern flank, the paleorift is bounded by the Nagar Parker fault (NPF) and Allah Bund fault (ABF), while on its southern flank, it is bounded by the Kachchh Mainland fault (KMF), South Wagad fault (SWF), Vigodi fault, and Katrol Hill fault (KHF). In past it has produced several moderate and major earthquakes, e.g., 1819 Allah Band earthquake (M 7.7), 1956 Anjar earthquake (M 6.0) and 2001 Bhuj earthquake (7.6).

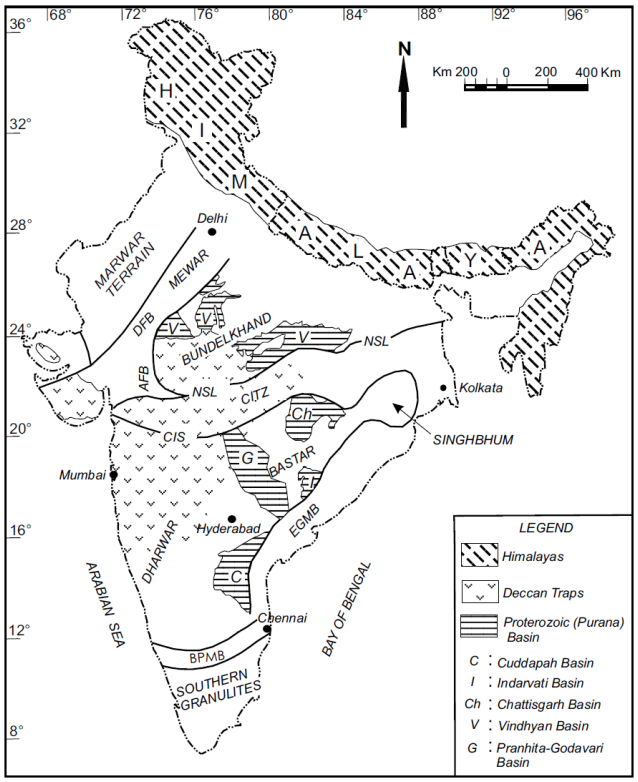

Figure 1.1: Generalized tectonic map of India: Precambrian mobile belts, lineaments, cratonic nuclei and Purana basins: AFB—Aravalli Fold belt, DFB—Delhi Fold Belt, CITZ—Central Indian Tectonic Zone, EGMB—Eastern Ghats Mobile Belt, BPMB—Bhavani-Palghat Mobile Belt, NSL—Narmada-Son Lineament, CIS—Central Indian Suture (Vijaya Rao and Reddy, 2002).

The east-west oriented Narmada-Son failed rift is probably the nearest earthquake source to the proposed Kalpasar dam. The Narmada-Son failed rift transects the peninsular shield area into the northern and southern blocks. It evolved during the Archean and Proterozoic period. Its episodic reactivation is evident by the presence of varied rock formations ranging in age from the late Archean to early Proterozoic Mahakoshal greenstone belt, punctured with geologic structures like the Vindhyan basin during Proterozoic, Gondwana basin of Palaeo-Mesozoic, possible fissures associated with the Deccan volcanism, and the Tertiary, Quaternary sedimentation in the Narmada valley. Two prominent deep faults called the Narmada South and Narmada North faults (NSF and NNF) with ENE-WSW strike have been mapped extensively in the region. These faults are on the boundary of Mahakoshal greenstone belt in the north and south. The presence of these faults have also been reported on the basis of deep seismic sounding studies. It has witnessed several moderate and strong magnitude earthquakes, e.g., 1927 Son valley earthquake (M~6.5), 1938 Satpura earthquake (M~6), 1970 Bharuch earthquake (M 5.4) and 1997 Jabalpur earthquake (M 6).

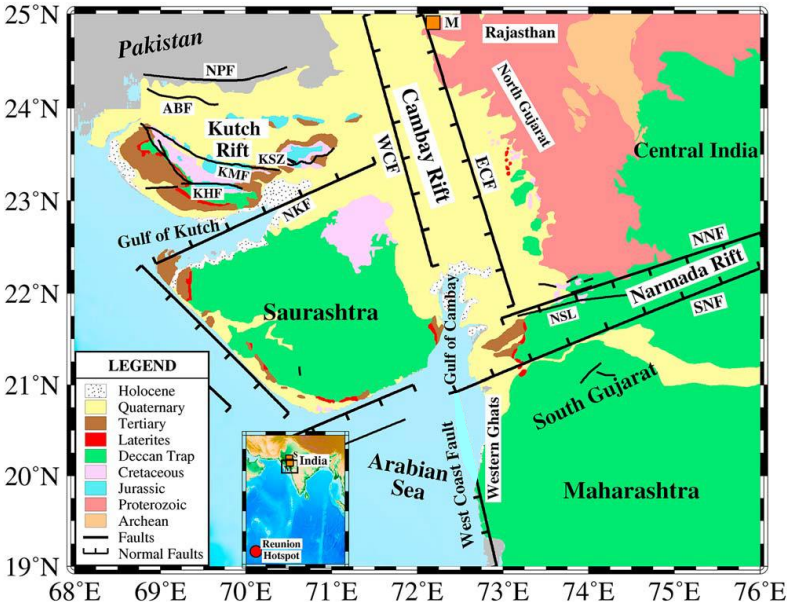

Figure 1.2: Geological and tectonic features of the northwestern Deccan Volcanic Province (DVP), India (modified after Biswas, 2005). The major faults in the study region are Nagar Parkar Fault (NPF), Allah Bund Fault (ABF), Kutch Mainland Fault (KMF), Katrol Hill Fault (KHF), North Kathiawar Fault (NKF), East Cambay Fault (ECF), West Cambay Fault (WCF), West Coast Fault (WCF), North Narmada Fault (NNF), South Narmada Fault (SNF), and Narmada-Son Lineament (NSL).

The NE-SW oriented Delhi Aravalli fold belt (ADFB) is another source which is to the north of the Kalpasar dam. Geographically, it is located in the north-western Indian Precambrian shield. The ADFB can be identified by the presence of the Palaeo-Proterozoic rocks of the Aravalli Supergroup in the south that are overlain by Proterozoic rocks of the Delhi Supergroup, the DS extends along the entire length of the ADFB from Mount Abu in the south to the Delhi-NCR region in the north. These fold belts are bounded to the west by the Malani Igneous Suite and that Marwar Supergroup that are both grouped together as the Trans-Aravalli Province. The ADFB uncomformably overlies the Banded Gneiss Complex and the Berach Granite that itself outcrops to the east of the ADFB. The BGC is the oldest Archean cratonic nucleus of the western Indian shield. Although the BGC is separated from the BKC in the Bundelkhand craton by Vindhyan cover rocks and the Great Boundary Fault (Sharma, 2009), they are thought to have undergone similar deformation events, shared similar geodynamic settings in the Proterozoic. The evolution of the ADFB has involved multiple stages of deposition, rifting, subduction, and orogeny. Based on interpreted structural features, such as the Jahazpur Thrust, and in combination with lithological and geochemical evidence, Vijaya Rao et al. (2000) present a model for the evolution of the AFDB that involves differential motion between the Marwar Craton to the west and the Bundelkhand Craton to the east (**Figure 1.2**) between ~1800 Ma and ~1100 Ma. Surface and subsurface geological structures associated with repeated phases of rifting subduction and orogeny have been mapped along the length of the ADFB between Delhi and Mount Abu (e.g., Vijaya Rao et al., 2000; Mandal et al., 2018). This region has experienced several moderate magnitude earthquakes, namely, the 1882,

1848, 1969, 2010 earthquakes in the Mt Abu and Udaipur region and 1762, 1956, 1960, 2003, 2012 earthquakes near Delhi-Jaipur region.

The above three are the most prominent source regions around the Kalpasar dam. The region to the west of the dam and south of the Kachchh failed rift, the Saurashtra region; the region to the southeast of the Kalpasar dam is covered with Deccan basalt. The region to the southwest of the Kalpasar dam is the old ocean floor and is generally devoid of earthquakes.

1.3 SEISMICITY OF THE REGION

Earthquakes from the global (ISC, USGS) and local (IMD/NCS) earthquake catalogues are combined and the duplicate events are removed. Catalogue containing 2095 shocks with M>2.0, was homogenized to Mw, and was declustered. A total of 677 aftershocks (32%) were identified which were removed. Thus the aftershock depleted catalogue contains 1418 mainshocks. Based on the geology and tectonics of the region around the Kalpasar dam, 6 zones were identified, namely, 1- Saurashtra; 2- Kachchh failed rift region; 3- ADFB and Vindhyan region; 4- Narmada Son failed rift region; 5- Deccan volcanic province; 6- Arabian sea (**Figure 1.3**).

The seismicity in the Kachchh region is most intense. This region has experienced at least two major earthquakes in historical past, the recent one in 2001 (M 7.6). The entire crust appears to be seismogenic, as seen from the focal depth of the earthquakes.

The Narmada Son failed rift region appears to be moderately active and has produced moderate to strong magnitude earthquakes. Even in this region, entire crust seems to be seismogenically active.

The Saurashtra, Deccan and ADFB & Vindhyan are less active and the seismicity appears to be confined in the upper crust (<15 km). The Arabian sea region appears to be least active.

Cambay rift has also been highlighted in the geological maps of India. However, it does not seem to be active, as seen from the seismicity map. Hence it is not considered here as a potential seismic source.

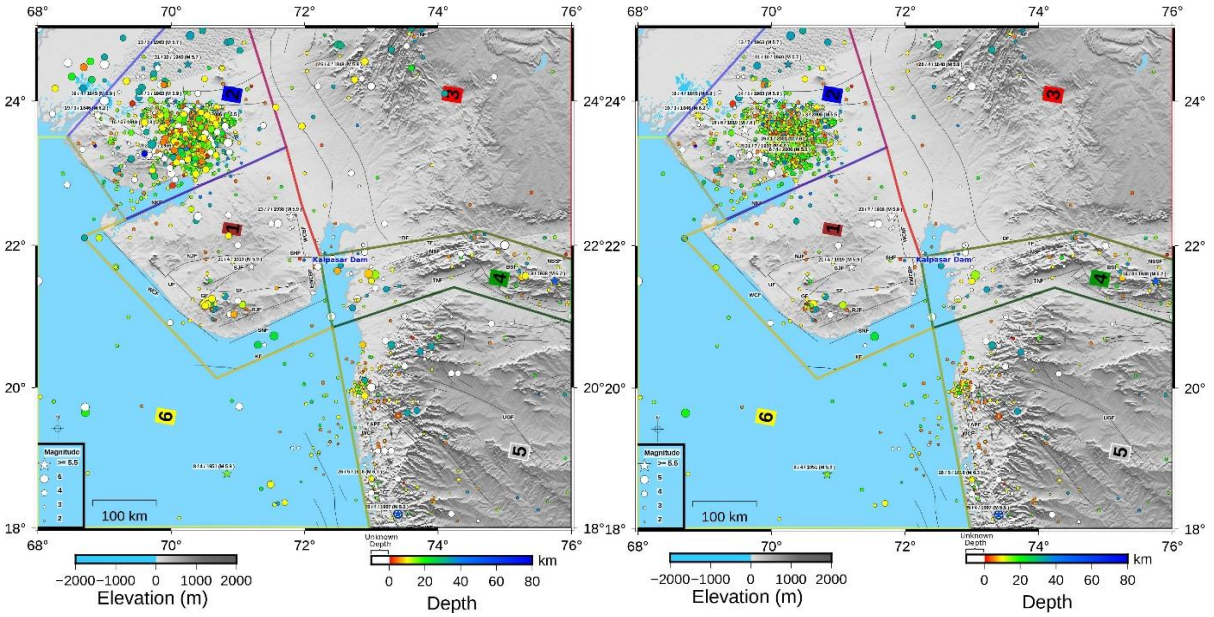

Figure 1.3: Seismicity of the region. Left panel shows earthquakes from all global and local catalogues. Right panel shows earthquakes compiled from various sources, after deleting the duplicate events, and verifying the magnitudes. Faults/lineaments are also plotted here. Based on the tectonics and earthquakes, the region is divided into 6 parts which are identified by the numbers.

Several estimates of focal mechanisms are available which are compiled in **Table 1.1** and **Figure 1.4**. However, several of them are not consistent with the Indian plate tectonics and several of them show large variations within a cluster. This is mainly due to limited number of stations used to constrain the focal mechanism solutions. These have been removed from the analysis and only those mechanisms have been considered which are reliable and are based on data from large number of stations (right panel of **Figure 1.4**).

Table 1.1: Focal Mechanism solutions for events M≥4. Solutions in bold are considered as reliable and are used here in the analysis.

Latitude	Longitude	Mw	depth	Strike1	Dip1	Rake1	Strike2	Dip2	Rake2	Date	Reference
ZONE 1											
20.98	**70.44**	**5.1**	**12**	**330**	**62**	**-172**	**236**	**83**	**-29**	**20/10/2011**	**GCMT**
21.04	**70.49**	**5.1**	**12**	**324**	**65**	**172**	**58**	**83**	**25**	**6/11/2007**	**GCMT**
22.157	70.888	4.8	11	153	86	180	243	90	4	16/7/2020	Kamra et al. 2021
ZONE 2											
23.4	**70.32**	**7.6**	**18**	**82**	**51**	**77**	**282**	**41**	**106**	**26/1/2001**	**Antolik and Dreger, 2003**
23.3	**70**	**6**	**15**	**235**	**47**	**85**	**62**	**43**	**85**	**19/2/1956**	**Chug and Gao, 1995**
23.61	**70.61**	**5.7**	**15**	**286**	**43**	**111**	**79**	**51**	**72**	**28/1/2001**	**GCMT**
23.25	**70.35**	**5.5**	**30.2**	**238**	**67**	**8**	**145**	**83**	**157**	**6/4/2006**	**GCMT**
23.72	**70.77**	**5.5**	**12**	**224**	**76**	**0**	**134**	**90**	**166**	**7/3/2006**	**GCMT**
23.72	**70.07**	**5.4**	**15**	**254**	**42**	**78**	**90**	**49**	**101**	**19/2/2001**	**GCMT**
23.74	**70.48**	**5.3**	**15**	**281**	**24**	**158**	**32**	**81**	**67**	**28/1/2001**	**GCMT**
23.64	70.29	5.1	10	102	86	163	194	73	4	19/6/2012	Kamra et al. 2021
23.52	**70.24**	**5.1**	**14.8**	**103**	**64**	**-179**	**13**	**89**	**-26**	**19/6/2012**	**GCMT**
23.68	**70.64**	**5**	**12**	**245**	**31**	**48**	**111**	**67**	**112**	**6/4/2006**	**GCMT**
23.69	**70.43**	**5**	**15**	**221**	**24**	**68**	**65**	**68**	**100**	**5/8/2003**	**GCMT**
23.36	**70.26**	**4.8**	**20.8**	**288**	**35**	**118**	**75**	**60**	**72**	**23/6/2006**	**GCMT**

23.23	70.54	4.7	27.8	73	44	102	236	48	79	28/3/2018	Kamra et al. 2021
23.72	69.91	4.6	8.5	153	65	-180	63	90	-25	28/10/2009	Nagabhushana et al. 2013
23.13	70.4	4.6	14	337	55	-136	218	55	-44	8/12/2012	Kamra et al. 2021
23.36	70.33	4.6	31	316	73	157	53	68	18	9/3/2008	Kamra et al. 2021
23.39	70.33	4.5	18	316	73	157	53	68	118	9/3/2008	Nagabhushana et al. 2013
23.3	70.09	4.5	11	130	74	134	236	46	23	8/10/2007	Nagabhushana et al. 2013
23.42	70.25	4.5	35	314	67	169	49	80	23	5/9/2009	Nagabhushana et al. 2013
23.43	70.42	4.4	13	320	72	175	52	85	18	13/5/2007	Nagabhushana et al. 2013
23.54	70.14	4.3	17	128	82	-32	223	58	-171	4/7/2016	Kamra et al. 2021
23.46	70.3	4.3	32	134	67	38	27	55	152	9/5/2015	Kamra et al. 2021
23.37	70.3	4.3	36	40	41	30	287	71	127	8/3/2014	Kamra et al. 2021
23.44	70.51	4.3	18	87	55	101	249	37	75	29/7/2013	Kamra et al. 2021
23.46	70.39	4.3	23	281	71	140	26	53	25	13/8/2011	Kamra et al. 2021
23.55	70.41	4.3	10	76	57	38	324	59	140	11/8/2010	Kamra et al. 2021
24.46	69.24	4.3	17	168	86	-4	258	86	-176	9/10/2009	Kamra et al. 2021
23.78	70.7	4.2	3	146	74	124	258	37	27	13/7/2007	Nagabhushana et al. 2013
23.37	70.38	4.2	19	101	35	96	274	56	86	8/4/2007	Nagabhushana et al. 2013
24	69.21	4.2	9	81	89	177	171	87	1	9/1/2017	Kamra et al. 2021
23.56	70.47	4.2	20	282	41	78	118	51	100	30/3/2013	Kamra et al. 2021
23.38	70.54	4.2	18	124	85	180	214	90	5	14/4/2012	Kamra et al. 2021
23.36	70.36	4.2	26	335	69	-165	240	76	-21	20/6/2008	Kamra et al. 2021
23.54	70.14	4.2	16	239	39	84	67	51	95	28/8/2007	Kamra et al. 2021
23.41	70.36	4.2	32	152	63	137	265	53	35	12/10/2006	Kamra et al. 2021
23.78	70.72	4.1	3	141	62	133	257	50	38	5/8/2007	Nagabhushana et al. 2013
23.4	70.14	4.1	16	42	49	33	289	66	134	12/4/2009	Nagabhushana et al. 2013
23.13	70.45	4.1	16	329	60	35	220	60	145	25/2/2018	Kamra et al. 2021
23.67	69.92	4.1	2	218	57	-28	324	67	-143	15/1/2018	Kamra et al. 2021
23.7	70.54	4.1	23	98	73	99	251	19	65	19/4/2014	Kamra et al. 2021
23.56	70.55	4.1	20	26	89	37	295	53	179	17/5/2011	Kamra et al. 2021
23.34	70.48	4.1	11	153	39	153	265	73	54	23/8/2010	Kamra et al. 2021
23.46	70.3	4.1	23	173	76	-176	82	86	-14	10/7/2008	Kamra et al. 2021
23.77	70.75	4.1	14	297	77	-178	206	88	-13	15/4/2008	Kamra et al. 2021
23.44	70.3	4.1	25	184	47	142	302	63	50	1/3/2008	Kamra et al. 2021
23.27	70	4.1	4	80	54	78	280	38	106	24/5/2007	Kamra et al. 2021

23.56	70.33	4	11	115	35	65	325	58	107	7/4/2008	Nagabhushana et al. 2013
23.4	70.43	4	19.3	242	51	9	146	83	141	10/3/2018	Kamra et al. 2021
23.43	70.14	4	16	360	57	-127	234	48	-47	23/8/2017	Kamra et al. 2021
23.58	70.29	4	11	182	80	178	272	88	10	13/6/2017	Kamra et al. 2021
23.45	70.56	4	21	70	24	96	243	66	87	7/12/2016	Kamra et al. 2021
24.28	69.72	4	13	332	81	-160	238	70	-9	2/9/2013	Kamra et al. 2021
23.33	70.1	4	29	279	67	161	16	73	24	11/9/2011	Kamra et al. 2021
23.45	70.38	4	7	307	63	9	213	82	153	23/2/2007	Kamra et al. 2021
ZONE 3											
24.76	**72.54**	**5.3**	**-**	**128**	**54**	**135**	**x**	**x**	**x**	**24/10/1969**	**Chandra, 1977**
23.82	71.97	4.2	12	300	63	-77	94	30	-114	2/9/2010	Chaudhury et al. 2019
24.54	72.03	4.1	9	223	46	-115	77	50	-66	13/3/2017	Chaudhury et al. 2019
ZONE 4											
21.6	**72.96**	**5.4**	**11**	**273**	**58**	**130**	**35**	**49**	**44.2**	**23/3/1970**	**Chung, 1993**
ZONE 6											
21.031	69.652	4.1	17	47	72	74	271	24	131	27/8/2016	Kamra et al. 2021

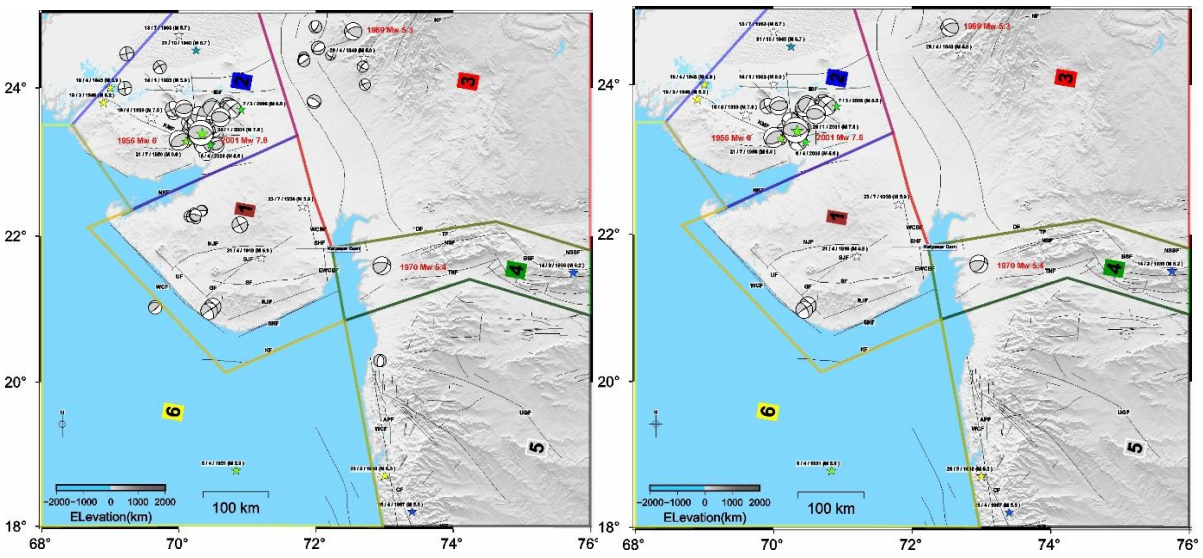

Figure 1.4: Earthquake focal mechanisms. Left panel shows the all available focal mechanisms in the region. Right panel shows the reliable and consistent focal mechanisms which are considered here for the analysis.

2.

Data analysis for deformation, strain & M_{max}

2.1 Crustal deformation and Strain rate

Available site velocity from 66 Indian shield GNSS sites which include 49 continuous and 17 campaign mode (Rajevar et al., 2021) were combined. Using site velocity in the stable India region, the Euler pole for India plate located at 51.992±0.22°N, 2.832±0.83°E with an angular velocity of 0.5205±0.002°/myr was estimated. Using this Euler pole, India's fixed site velocity was estimated. The two-dimensional strain rate was calculated using the site velocity estimates in the stable Indian region where dilatational, second invariant, principal axes, and maximum shear strain rate were calculated. The plate interior region, in general, exhibit significantly lower shear strain rate (~1-3 μstrain/yr), while the Kachchh region exhibit higher shear strain rate (~9 μstrain/yr) (**Figure 2.1**). In **Figure 2.2** shows the strain rate in and around the Kalpasar dam. It appears that the shear strain rate are ~1 nanostrain/year in the Kalpasar dam region.

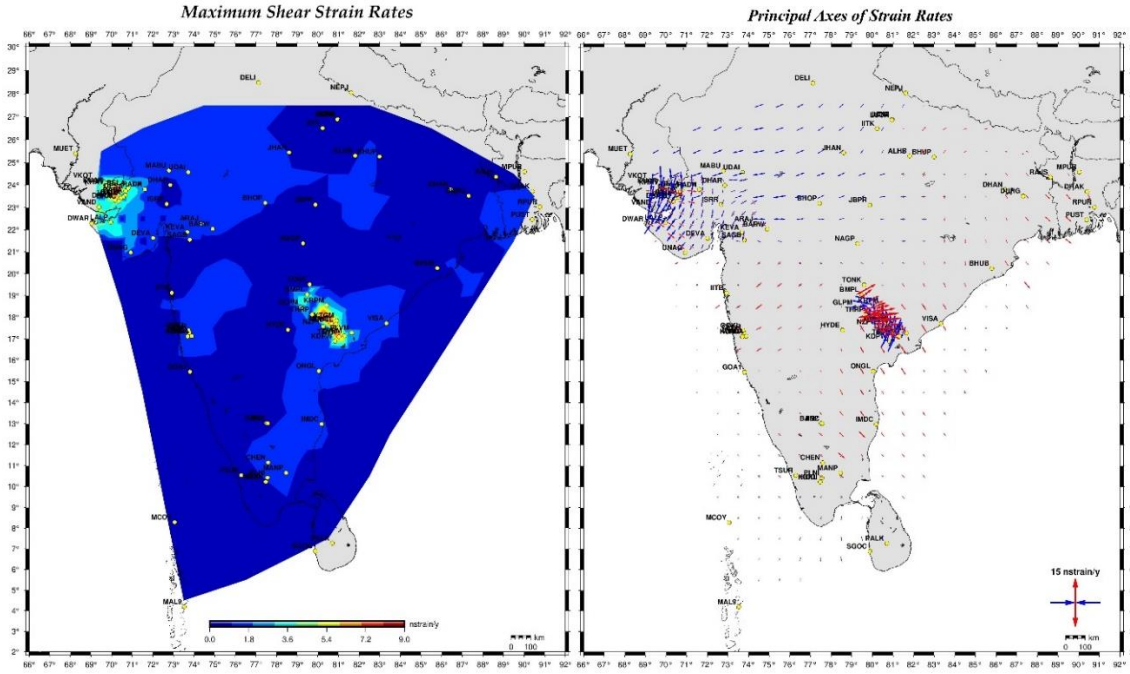

Figure 2.1: Maximum shear strain rates and direction of principal axes from GPS observations (yellow circles are GPS sites).

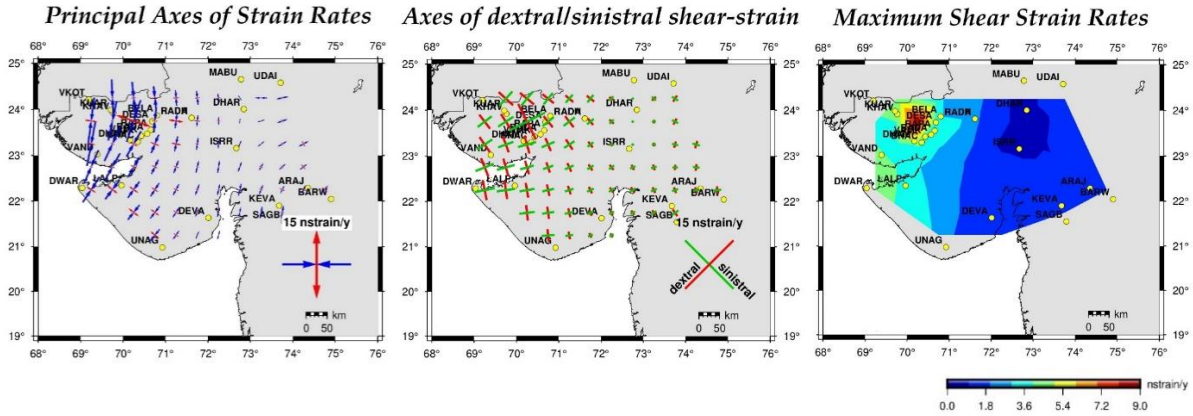

Figure 2.2: Magnitude and direction of strain in the Kachchh, Saurashtra, Naramada Son and ADFB, derived from GPS observations (Gahalaut et al., 2019).

To further confirm the low and insignificant strain rate in the Kalpasar region, InSAR analysis was undertaken.

2.2 InSAR analysis of deformation

In recent years, remote sensing has been applied to dam surveillance, specifically the technique of Interferometric Synthetic Aperture Radar (InSAR), where ground movements can be monitored with high precision. The potential for this technology to enhance dam safety by providing timely settlement measurements in high spatial resolution has been demonstrated in several studies. For dam safety applications, the reliability and consistency will have to be tested prior to InSAR being broadly adopted among more traditional trusted and conventional methods

On 3rd April 2014, ESA launched the first Sentinel-1 (S1) satellites with the interferometric wide swath (IWS) mode selected as the primary acquisition mode. In IWS mode, the data are acquired using the so-called TOPS mode. TOPS stands for Terrain Observation with Progressive Scans in azimuth. One of the strengths of the IWS mode is the wide swath width of about 250km. S1 is operated at C-band with an orbit repeat cycle of 12 days (Wegnüller, 2016). Gamma InSAR software was used in the present study to derive differential interferometry and spatio-temporal time series analysis (Interferometric Point target analysis IPTA) for the Kalpasar Dam region.

2.2.1 Input data:

Sentinel-1 (S1) IWS data are available as RAW, SLC (Single Look Complex) and GRD (Ground Range Dataset) products. S1 IWS RAW data are distributed for specific usage only. In this work, Sentinel – 1A SLC data sets are used to comprehend spatial and temporal deformation in Kalpasar Dam region. 22 scenes of C-Band Sentinel-1A SLC (Single look complex) datasets acquired during descending orbit pass spanning from March 2020 to December 2020 was used (**Figure 2.3**).

Details of Data:

1) SAR: Sensor : Sentinel-1A single look complex data
   Band : VV
   Beam Mode : IWS(Interferometric wide swath)
   Time period : 22-03-2020 to 23-12-2020
   total scenes : 22
2) Precise Orbit files: AUX_POEORB.EOF files
3) Digital Elevation Model: DEM: SRTM 1-arcsecond (30-meter)

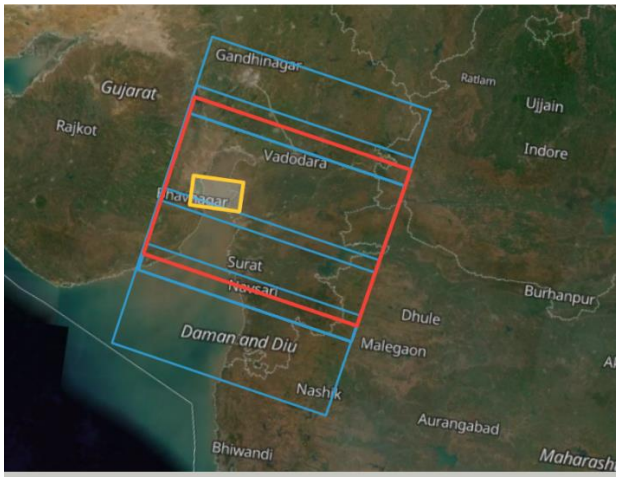

Figure 2.3: Study area

2.2.2 Methodology:

Differential Interferometric Synthetic Aperture Radar (DInSAR) **:**

Sentinel-1 constellation has been specifically designed to perform over a land, advanced DInSAR analyses for the investigation of Earth's surface displacements. In the DInSAR Processing, the SLC images were coregistered to a common geometrical master. Later, an area of interest was selected to perform multilook processing, the Geocoding transformation between Radar coordinates and Ground coordinates. To convert Geo-coordinates to Radar coordinates, DEM SRTM 1-arcsecond (30-meter) data was used. Finally, phase filtering process was applied to generate differential interferograms. Interferograms are images of relative ground-surface change that are constructed from InSAR data to understand how tectonic or anthropogenic events, such as groundwater extraction and hydrocarbon production, cause the land surface to uplift or subside. If the ground has moved away from (subsidence) or towards (uplift) the satellite between the times of the two SAR images, a slightly different portion of the wavelength is reflected back to the satellite resulting in a measurable phase shift that is proportional to displacement. Several differential interferograms have been tested for the one-year data in different pair images. **Figure 2.4** shows relative displacement between the first and second acquisitions and the different colours represent the different phase values from -π to π. The Image (**Figure 2.4**) not

showing any systematic fringes near dam and adjoining regions due to lack of deformation in this region

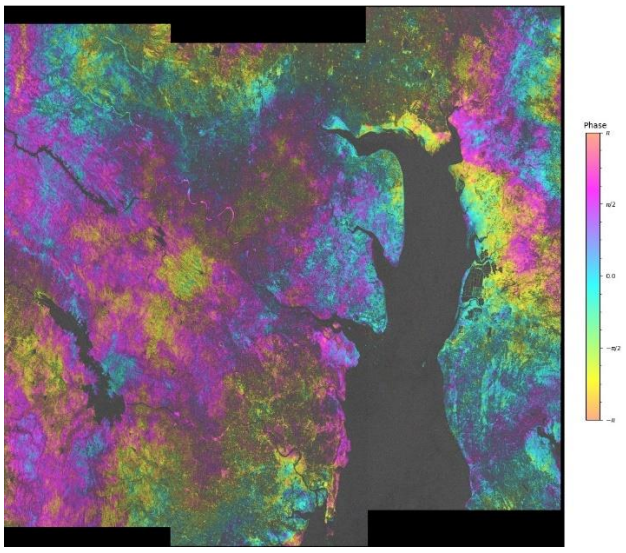

Figure 2.4: Sentinel-1A Differential Interferogram of the study area and acquisitions collected from March 2021(202103-05_2021-03-17). An interferogram is created by using two SAR images acquired at two different times and mapping the phase shift caused by a movement of the surface between the two acquisitions. Radar wavelength is represented by a phase (pi) in radians.

2.2.3 Multi-Temporal:

Gamma interferometric point target analysis (IPTA) was used in the multi-temporal technique in the present study. The phase model used for the IPTA is the same as conventional interferometry. The unwrapped interferometric phase is expressed as the sum of a topographic phase, a deformation phase, a differential path delay phase (also called atmospheric phase), and phase noise (or decorrelation) terms. The interferograms are interpreted for the selected points. Point data stacks in vector format are used for interferograms, unwrapped phases, topographic heights, deformation rates, residual phases associated with the atmosphere, and others. An additional data vector is used to save the point coordinates. Specific programs support the conversion between vector and raster data formats.

An important aspect of IPTA is that for point targets, no spatial decorrelation occurs, permitting interpretation of the interferometric phase of pairs with long baselines, even above the critical baseline. Based on these ideas, one crucial objective of the IPTA is to achieve a complete use of the available data. Through point targets, interferometric pairs with long baselines can be used (Gamma Rs Software IPTA_users_guide for further reading). The flow chart (**Figure 2.5**) shows the processing sequence of IPTA analysis.

Processing Sequence of IPTA Method

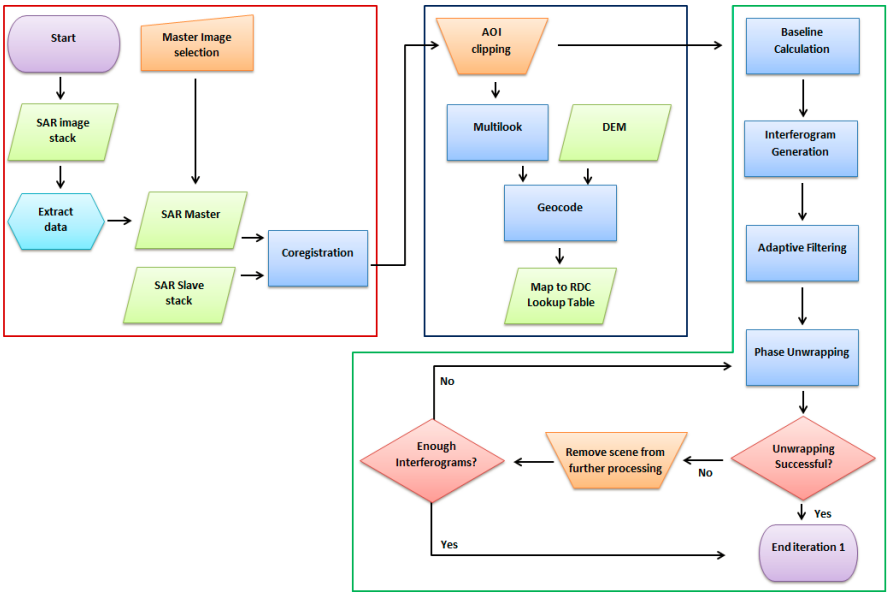

Figure 2.5: Flowchart of iteration 1, which consists of three stages. In stage 1 (red block), the SLC images are extracted, a geometrical master (Primary Image) selected, and the secondary images coregistered to this master. In stage 2 (green), the study area is clipped from each of the coregistered SLC's, multi-looking is performed, and the geocoding transformation established. In stage 3, baselines are calculated and a corresponding suite of filtered, unwrapped, differential interferograms generated.

In order to create a stacked deformation map (**Figure 2.6**) from an unwrapped interferogram, phase values must first be converted to displacement (in meters). This displacement value is derived from the differential phase values in the line of sight of Sentinel-1. **Figure 2.6** is one of the study region's deformation maps and it does not show any significant deformation near the dam region.

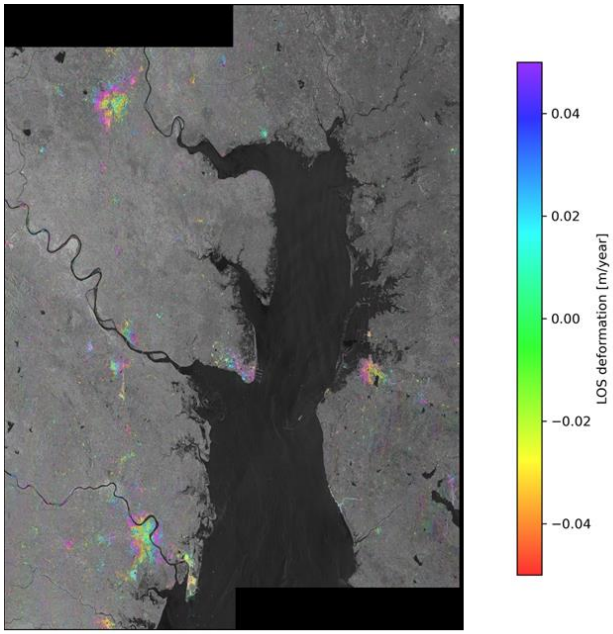

Figure 2.6: The stacked Images S1A of Line-of-Sight Deformation (LOS) of the Kalpasar Dam and surrounding regions based on the IPTA method**.**

2.2.4 Multi-Temporal Interferometric Point Target Analysis Results.

Using a significant number of differential interferograms, the deformation time series was generated to investigate the study region's temporal and spatial behaviour.

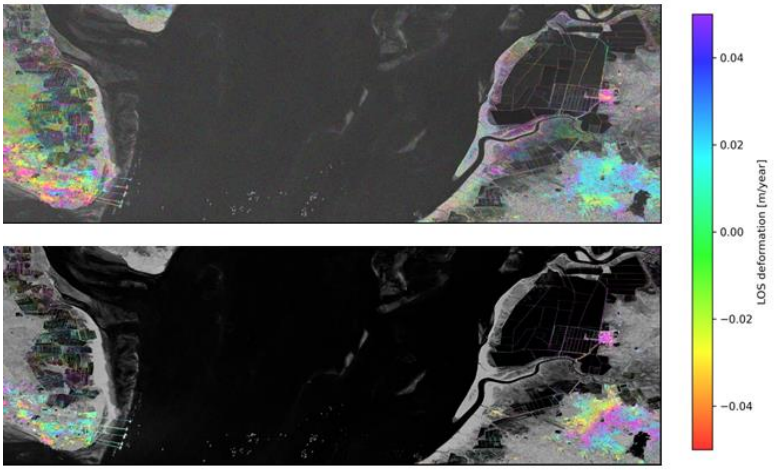

Figure 2.7: Rate of deformation points derived from the stacked differential interferogram. The top panel shows points derived based Multi look stacked images, and the bottom panel shows Single look stacked images, both obtained from IPTA Module. Different colors represent different deformation rates.

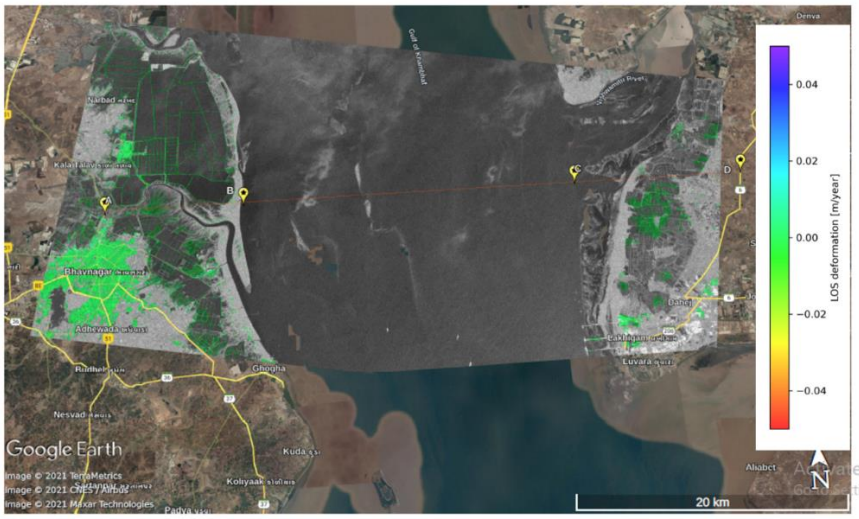

Figure 2.8: Geocoded rate of deformation (**Figure 2.6**) superimposed over a Google Earth image. It shows there is no deformation in the Kalpasar dam location.

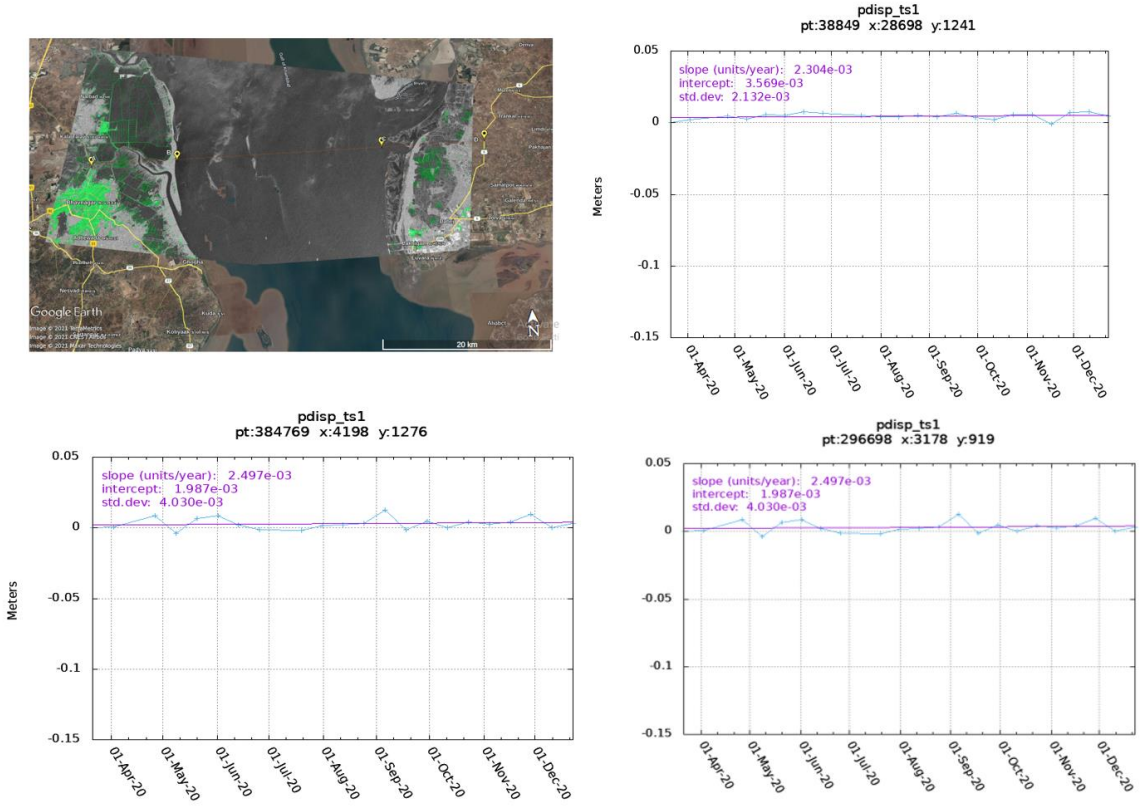

Figure 2.9: Deformation time series corresponding to three different points obtained from IPTA**.**

2.2.5 Summary of InSAR analysis

In this study, 22 Sentinel 1A SLC images were used to study for one year of data based on DInSAR and IPTA InSAR Time series analysis to study the rate of deformation in the Kalpasar dam region Gujarat. Based on DInSAR and IPTA analysis, the obtained

results do not show any significant deformation in the Kalpasar dam region, consistent with the GPS results (**Figures 2-7-2.9**).

2.3 'b' value (Gutenberg and Richter relation)

To estimate the design seismicity for hazard analysis, the following form of Gutenberg-Richter's (1956) magnitude-frequency relationship is defined for all the seismic source zones in the region of the project using the available past earthquake data

$$\log N(M) = a - bM \qquad \textbf{(2.1)}$$

In this expression, *N(M)* is the cumulative annual number of earthquakes with magnitude *M* or greater, and *a* and *b* are the empirical constants determined by regression analysis of past earthquake data. To estimate the parameters *a* and *b* in eqn. (1), the earthquake catalog homogenized to the moment magnitude is declustered to remove fore- and after-shocks and completeness analysis is carried out for the data in each source zone to identify the period of completeness in different magnitude ranges. The widowing method due to Gardner and Knopoff (1974) with the distance and time widows selected as per Uhrhammer (1986) has been used for the purpose of declustering the catalog in the present study. The periods of completeness for different magnitude ranges in each source zone are then estimated using a method due to Stepp (1973). Parameters *a* and *b* for each source zone are estimated by maximum likelihood method of Weichert (1980) using the completely recorded data in different magnitude groups. Typical fitting of the recurrence curves to the observed recurrence rates for all the source regions are shown in **Figure 2.10**. Observed data is plotted with mean and plus and minus one standard deviation bars.

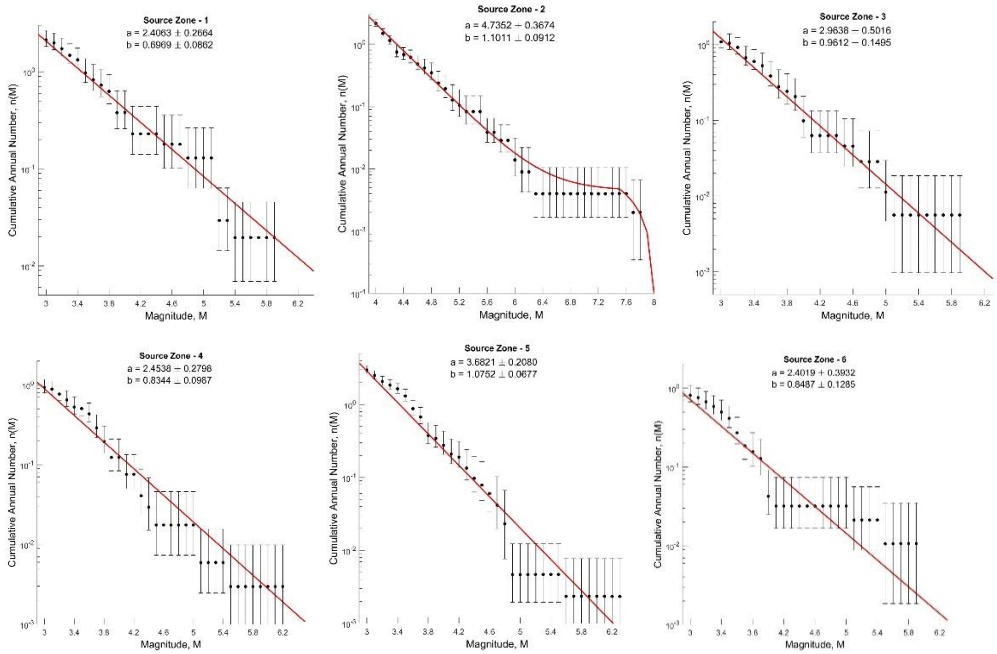

Figure 2.10: b value estimation in the six identified source zones. Red line in each graph represent the Gutenberg Richter relation (log N = a-bM). In source region 2, only the linear part is considered.

2.4 Estimation of Maximum magnitude (M_{max}) in the source zones

There are several methods of estimating M_{max} for a seismic source zone (SSZ). The M_{max} is required to define the maximum credible earthquake (MCE) ground motion in the DSHA method and to put an upper limit on the Gutenberg-Richter (G-R) relation in the PSHA method. M_{max} for each source zone is estimated by applying all possible methods (as given below).

a) Judicious enhancement of observed M_{max}: In this method, the M_{max} is obtained simply by increasing the largest observed earthquake magnitude, M_{max}^{obs} in a source zone by 0.5 to 1.0 magnitude units in a purely subjective way.
b) Extrapolation of GR relationship: Due to limited duration of the earthquake catalog, it is generally unlikely that the largest possible magnitude in a source zone already exists in the available catalog. Extrapolation of the frequency magnitude relation developed using the catalog data to a longer period may thus be used to get an estimate of the M_{max} (Bollinger et al., 1992; Wheeler, 2009).
c) Statistics of largest magnitude earthquakes: Dargahi-Noubary (1999) has proposed to estimate the M_{max} from knowledge of the magnitudes of a few highest magnitude earthquakes and an approximate knowledge of the total number of events available in the catalog. If n is the total number of events and $M_1, M_2, \ldots, M_n$ are their magnitudes arranged in decreasing values, then M_{max} with a confidence level p can be defined by

$$M_{\max} = M_1 + \frac{(M_1 - M_2)}{p^{-\alpha} - 1}; \quad \text{with } \alpha = \frac{\ln k}{(M_3 - M_k)/(M_2 - M_3)}$$

where k=[√n] is the largest integer less than or equal to the number within the brackets.

d) Mixed data probability distribution: Kijko (2004) have developed methods for getting the maximum likelihood estimates of the mean seismic activity rate λ, b-value in the G–R relation, and the M_{max} using mixed probability distributions for all the three parameters. Both, the incomplete and complete parts of the catalog with different magnitudes of completeness are used for the estimation of these parameters with their uncertainties accounted by Bayesian probability distributions. Kijko et al. (2016) have developed a MATLAB program to implement this method, which has been used to estimate the M_{max} in our cases.

e) Cumulative energy release Benioff plot: Earthquakes in a seismic source zone are generated by sudden release of the strain energy stored at a very slow rate over long period of time. The plot of the cumulative strain energy released in the form of earthquakes as a function of time is known as the Benioff plot, which can be used to estimate the probable maximum magnitude in a source zone as described in Makropoulos and Burton (1983). The energy E_i released by ith earthquake in the catalogue with magnitude M_i can be estimated from the relationship $\log E_i=1.5M_i+11.8$ due to Gutenberg and Richter (1956).

f) Fault rupture length: By compiling a database on the observed rupture parameters of 77 worldwide earthquakes, Wells and Coppersmith (1994) have developed empirical relations between earthquake magnitude, M_W, and the surface rupture length of the fault, L, in km for different types of faults. These relations can be used to estimate the maximum magnitude for a specific fault, provided the maximum length of the fault that may rupture during a future earthquake is known with good confidence. However, the rupture length of expected future earthquake cannot be defined with any accuracy. In practical applications, the maximum rupture length is generally taken as small fraction of the total length (e.g., Mark, 1977; Slemmons, 1982; etc), which should vary with the total fault length in a region specific manner (Anbazhagan et al., 2015). In practical applications, it is commonly assumed that a maximum of 1/3rd of total fault length can rupture during a single earthquake (Kayabalia and Akinb, 2003). This method cannot be applied to the area sources and tectonic provinces, because the individual faults and their rupture parameters are difficult to identify.

Unfortunately, fault rupture length is not available from all the regions and hence was not considered it in estimation of M_{max}.

g) Strain rate from GPS measurements: The global strain rate data given by Kreemer et al. (2014) can be used to estimate the scalar moment rate, Mo, for an area source (Kostrov, 1974), which in turn can be used to estimate the M_{max} from knowledge of the G-R parameters a and b using the following expression.

$$\dot{M}=\left(\frac{c}{c-b}\right)\times 10^{a-bM_{max}}\times 10^{cM_{max}+d}$$

Kreemer et al. (2014) have given the principal components ε_1 and ε_2 of the strain rates for grid cells of size 0.25°× 0.20° in latitudes and longitudes for the entire globe, which can be used to define the scalar moment rate, δMo, for a grid cell using

$$\delta\dot{M}_0 = 2\mu\mu H\delta A\ \max\left(|\varepsilon_1|,|\varepsilon_2|,|\varepsilon_1+\varepsilon_2|\right)$$

where μ is the modulus of rigidity, H is the thickness of the seismogenic layer, δA is the area of the grid cell, and the function max is equal to the largest of its arguments.

Taking $\mu=3.0x10^{11}$ dyne/cm^2 and the seismogenic thickness H as 15 km on the basis of the average focal depths of past earthquakes, the sum of the moment rates for all the grid cells in the source zones can be calculated.

Using above methods, the M_{max} for each source zone was estimated and then finally decided on the most appropriate value used in the calculations (**Table 2.1**).

Table 2.1: Estimation of M_{max} using the seven methods listed in section 2.4 in each source zone

S.No.	Name of Source Zone	M_{max} in the catalogue	Values of M_{max} obtained by method number							M_{max} used
			a)	b)	c)	d)	e)	f)	g)	
1	Saurashtra Horst	5.9	6.2	7.8	5.9	6.2	5.9	–	6.3	6.3
2	Kutch Rift Basin	7.8	8.0	–	7.9	8.4	7.8	–	6.7	8.0
3	Northern Peninsular Shield	5.9	6.2	6.2	6.1	6.2	5.9	–	–	6.2
4	Son-Narmada-Tapi Basin	6.2	6.4	6.5	6.6	6.4	6.2	–	–	6.5
5	Deccan Traps Province	6.3	6.5	6.2	6.4	6.7	6.3	–	–	6.5
6	Arabian Sea Zone	5.9	6.2	6.4	6.2	6.4	5.9	–	–	6.4

2.5 Source characterization for scenario earthquake using the available data and analysis

Based on the available geological data, spatial distribution of earthquakes, their focal depths and focal mechanisms, and above calculations of M_{max}, following representative parameters for the scenario earthquakes in each source zones have been estimated. For the calculations of the fault length, Wells and Coppersmith (1994) relations have been used.

Table 2.2: Source characterization for scenario earthquake in each source zone

S.No.	Source Zone	Considered Focal Depth (km)	Preferred Range of Strike Angle	Preferred Dip Angle	Predominant Type of Faulting	Length (km)
1	Saurashtra Horst	12	325 (D), 60 (S)	70	Strike slip	22
2	Kutch Rift Basin	20	80 (R),	50	Reverse	166
3	Northern Peninsular Shield	20	130(D)/250(S)	55	Oblique (SS+R)	17
4	Son-Narmada-Tapi Basin	15	270	60	Oblique (R+SS)	26
5	Deccan Traps Province	8	180	60	Strike slip	29
6	Arabian Sea Zone	15	50/270	75/25	Oblique (R+SS)	22

D- Dextral strike slip, S- Sinistral strike slip, R- Reverse, SS- Strike slip.

2.6 Geotechnical characterization of the region

V_{S30} values were provided by the NCCR at four sites, and they were used as they were without any alteration. No other geotechnical data were used in this report.

3. Deterministic Seismic Hazard Assessment

3.1 INTRODUCTION

This section describes the major inputs to the site-specific *Deterministic Seismic Hazard Analysis (DSHA)* including characteristics of the nearby faults, selection and weighting of *Ground Motion Models (GMMs)*, and recommended earthquake ground motions for the MCE at the dam location.

DSHA uses available seismic and geological data to generate discrete, single-valued earthquakes to model ground motions at a site. It is a methodology to evaluate the *Maximum Credible Earthquake (MCE)* that will generate the most severe ground motions at the site. DSHA requires identification and characterization of the major seismic sources such as seismogenic faults. Earthquakes generated at these sources are evaluated to identify the MCE. These maximum earthquakes are specified by their magnitudes and source-to-site distances. Usually, the earthquakes are assumed to occur on the portion of the fault closest to the site.

Empirical GMMs (attenuation relations) are used to establish the site ground motion given the earthquake magnitude, source-to-site distance, and site ground conditions. A key feature of DSHA is that it does not explicitly consider the recurrence interval for the MCE ground motions. The median (50^{th} percentile) spectral accelerations from the DSHA is commonly used to represent the MCE ground motions.

3.2 SITE LOCATIONS AND SITE GROUND CONDITIONS

Seismic hazard is estimated at four locations along the dam, where surface wave testing (PS-logging tests) were conducted. These locations have well-documented site characterization and hence are useful in the accurate estimation of hazard. The site locations where hazard will be calculated are shown in **Table 3.1**.

For earthquake ground motion studies, the time-averaged shear-wave velocity in the upper 30 m below the ground surface (i.e. V_{S30}) is a typical proxy for the site ground condition. A number of GMMs scale with the V_{S30} value, so it is important that the final earthquake ground motions are calculated using a realistic estimate of the V_{S30} at the sites. For the purpose of hazard assessment, V_{S30} is calculated using the PS-logging results provided by *ACES*. V_{S30} values for each of the locations, where hazard needs to be estimated, is also shown in **Table 3.1.**

Table 3.1: Locations and V_{S30} of the sites used in this hazard estimation

Site	Latitude (°N)	Longitude (°E)	V_{S30} (m/s)
PS1	21.8070	72.1886	339
PS2	21.8072	72.3409	420
PS3	21.8072	72.4920	434
PS4	21.8072	72.5494	483

3.3 FAULT SOURCES

The area considered for the purpose of hazard assessment is bound by 18° - 25° N and 68° - 76° E, as discussed in the previous sections (**Section 1.3**). The region is divided into six seismic source zones, as shown in **Figure 1.3**. MCE is calculated at each of the source zone using a variety of statistical methods proposed in the literature [Bollinger et al., 1992; Wheeler, 2009; Dargahi-Noubary, 1999; Kijiko et. al, 2004; Makropoulos-Burton, 1983; Wells-Coppersmith, 1994; Kreemer et al., 2014]. Various possible worst-case scenarios are considered for the purpose of hazard assessment.

As discussed in Chapter 1 (section 1.3), seven earthquake potential zones have been identified around the Kalpasar dam. In each case the maximum possible size of the earthquake was estimated. For each source zone the location of the scenario earthquake rupture on one extreme of the zone which is closest to the Kalpasar dam was assumed. In zone 1 (Saurashtra), the longest and nearest reported fault is located on the southern coast of Saurashtra, and its eastern end which extends upto ~72°E longitude was considered. In zone 2 (Kachchh region) the scenario earthquake on the eastern extent of the Kachchh Mainland fault was considered. In zone 3 (Delhi Aravalli fold belt) the scenario earthquake to be located on the southern edge of the Delhi Aravalli fold belt was considered. In zone 4 (Narmada Son failed rift region), the scenario earthquake on the western edge of the fault which is dipping towards north was considered. In zone 5, although no potential faults are identified, the scenario earthquake on the northern extent of the Koyna Warna fault zone was considered. In zone 6 (Arabian sea) for which no information on the mapped faults is available, the location of the 1951 earthquake for which fault parameters were assumed similar to zone 1 was considered. In the last case, a scenario earthquake was assumed right below each site with fault parameters similar to zone 4, assuming it to be the continuation of that zone. Although such a case is unlikely as the Narmada Son failed rift region may not be extending to farther west, this case provides a most conservative estimate of seismic hazard at site. The scenarios along with the MCE calculated for each seismic source zone and their expected fault location is summarized in **Table 3.2**.

Table 3.2: MCE and location of the expected MCE for each worst-case scenario

Scenarios	MCE	Location of the expected MCE
1	6.3	Coastal fault on the south coast of Saurashtra
2	8.0	Kuchchh failed rift
3	6.2	Southern most mapped fault of the Aravalli Delhi fold belt
4	6.5	Western most part of the Narmada failed rift
5	6.5	Northern extent of the Koyna-Warna fault zone
6	6.4	Epicenter of 8/4/1951 earthquake
7	5.2	Below each of the site locations

The major characteristics of these fault zones along with their fault plane solutions used for each of these scenarios for hazard calculations are shown in **Table 3.3.** For estimating the length and width of the scenario earthquake rupture of M_{max}, relations from Wells and Coppersmiths [1994] were used. For depth, strike, dip and mode of faulting, the information from seismicity and seismotectonics part was used.

Table 3.3: Characteristics of the fault zones along with their fault plane solutions

Scenarios	Length (km)	Width (km)	Depth (km)	Strike Angle (°)	Dip Angle (°)	Predominant Faulting
1	22	9	12	60	70	Strike-Slip
2	166	47	20	80	50	Reverse
3	17	8	20	130	55	Strike-Slip
				250		
4	26	11	15	270	60	Reverse
5	29	10	8	180	60	Strike-Slip
6	22	10	15	50	75	Reverse
				270	25	
7	4.2	3.9	10	270	60	Reverse

3.4 GROUND MOTION MODELS (ATTENUATION RELATIONS)

GMMs are used in seismic hazard analysis to estimate the source-to-site attenuation of earthquake ground motions at PGA and at other spectral periods (usually 5%-damped). The GMMs used in this study were selected based on the similarity between tectonic conditions surrounding the dam site. Two PEER Next Generation of Ground Motion Attenuation Phase 2 Project (PEER NGA-West2 Project) GMMs were used in this study for earthquake ground motion calculations for all seismic sources. The NGA-West2 GMMs were developed for active tectonic regions based mostly on the earthquake strong ground motion data recorded at seismically active, present-day plate boundaries, primarily from the Western United States and around the world. These NGA-West2 GMMs were chosen due to lack of appropriate GMMs in the area of study and for the global inclusivity of these NGA-West2 GMMs.

The two NGA West2 GMMs – Abrahamson et al. (2014) and Boore et al. (2014) were weighted equally (i.e., 0.50 each) while being used in this study. The various

distance parameters used in these GMMs, for each of the site locations are shown in **Table 3.4** through **Table 3.7**.

Table 3.4: Distance parameters used in the GMMs for site location PS1

Scenarios	R_{RUP} (km)	R_{JB} (km)	R_X (km)	R_{Y0} (km)
1	80.7	80.3	-64.2	59.6
2	192.4	188.6	204.0	73.6
3	323.0	322.1	-271.4	178.5
	326.6	326.1	-298.7	134.5
4	81.1	78.6	24.3	76.4
5	339.2	339.0	85.7	329.2
6	353.7	353.6	-167.7	353.6
	351.8	351.4	335.9	129.1
7	8.3	0.0	1.0	0.0

Table 3.5: Distance parameters used in the GMMs for site location PS2

Scenarios	R_{RUP} (km)	R_{JB} (km)	R_X (km)	R_{Y0} (km)
1	84.0	83.6	-56.3	73.4
2	201.2	197.6	206.4	89.2
3	321.6	320.7	-261.5	188.3
	326.3	325.9	-303.8	118.9
4	66.5	63.5	24.3	60.7
5	336.2	336.0	69.6	329.2
6	360.0	359.8	-157.6	359.8
	358.0	357.6	335.9	144.9
7	8.3	0.0	1.0	0.0

Table 3.6: Distance parameters used in the GMMs for site location PS3

Scenarios	R_{RUP} (km)	R_{JB} (km)	R_X (km)	R_{Y0} (km)
1	90.2	89.9	-48.5	86.8
2	210.7	207.2	209.0	104.7
3	320.8	319.9	-252.1	200.0
	325.9	325.5	-306.8	103.9
4	52.7	48.8	24.3	45.0
5	333.2	333.0	53.8	329.2
6	366.8	366.6	-147.7	366.6
	364.9	364.5	335.9	160.4
7	8.3	0.0	1.0	0.0

Table 3.7: Distance parameters used in the GMMs for site location PS4

Scenarios	R_{RUP} (km)	R_{JB} (km)	R_X (km)	R_{Y0} (km)
1	92.9	92.6	-45.6	92.2
2	214.5	211.1	209.9	110.5
3	321.2	320.3	-248.5	207.4
	326.1	325.7	-310.6	98.9
4	47.7	43.4	24.3	39.0
5	332.2	332.0	48.0	329.2
6	369.5	369.3	-144.0	369.3
	367.6	367.2	335.9	166.5
7	8.3	0.0	1.0	0.0

3.5 TARGET RESPONSE SPECTRA

3.5.1 Median Target Response Spectra (50th percentile)

The various scenarios mentioned in **Table 3.2** are used in order to determine the critical scenario, which will provide the most conservative results for each dam site location. The *median response spectra* (50th percentile) obtained from both the GMMs weighted equally is hence calculated.

The median response spectra are shown for different cases as mentioned in **Table 3.2** for all the 4 site locations in **Figure 3.1**. As seen from the median response spectra from all the four locations, the low-magnitude earthquake of M = 5.2 under the dam location (near distance) dominates in the lower periods, whereas the high magnitude earthquake of M = 8.0 at a farther distance will dominate in the long period spectrum. Hence, the combination of the two magnitudes should be jointly used to determine the critical scenario in each case. The joint combination or *envelope* of the low magnitude earthquake at a shorter distance and high magnitude earthquake at a farther distance is shown in **Figure 3.2**.

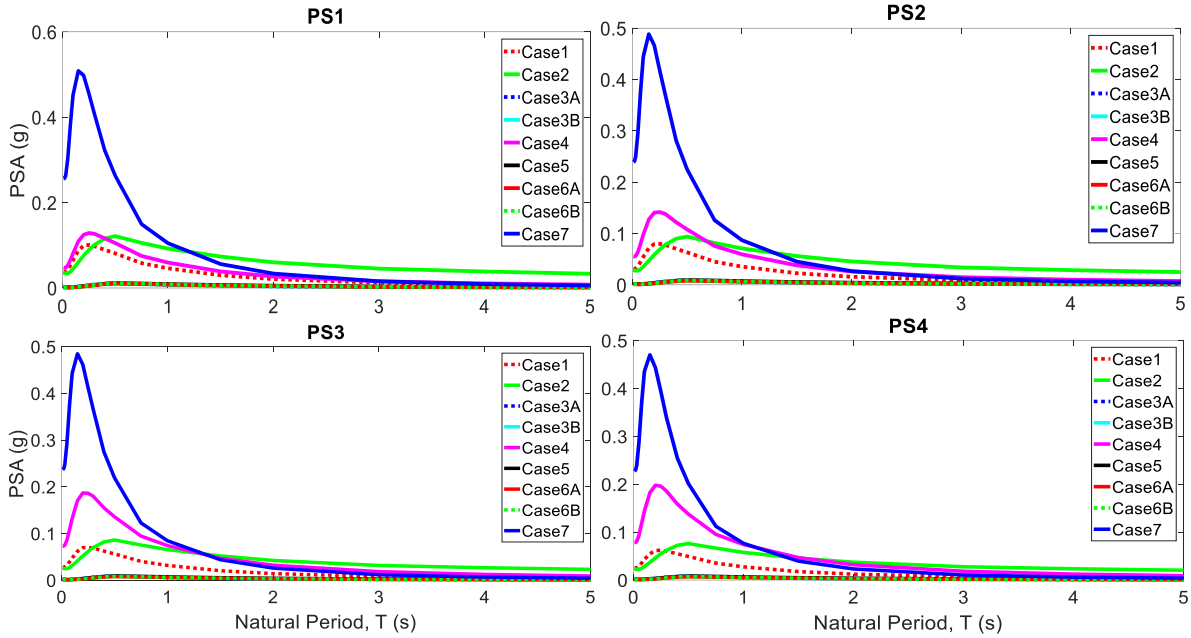

Figure 3.1: *Median Target Response Spectra* (50th percentile) of various scenarios for the four dam locations

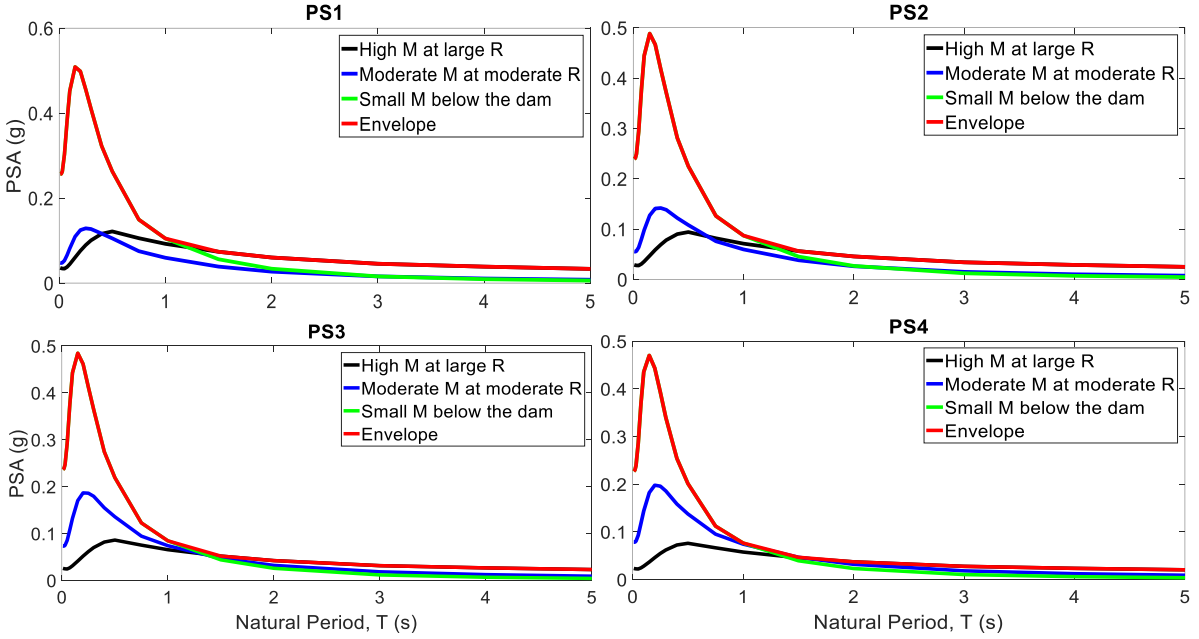

Figure 3.2: *Envelope Median Target Response Spectra* (50th percentile) considering critical scenarios for the four dam locations

Hence, the envelope in **Figure 3.2** is taken to be the target response spectra for the 50th percentile calculated from the DSHA method and is shown separately in **Figure 3.3**.

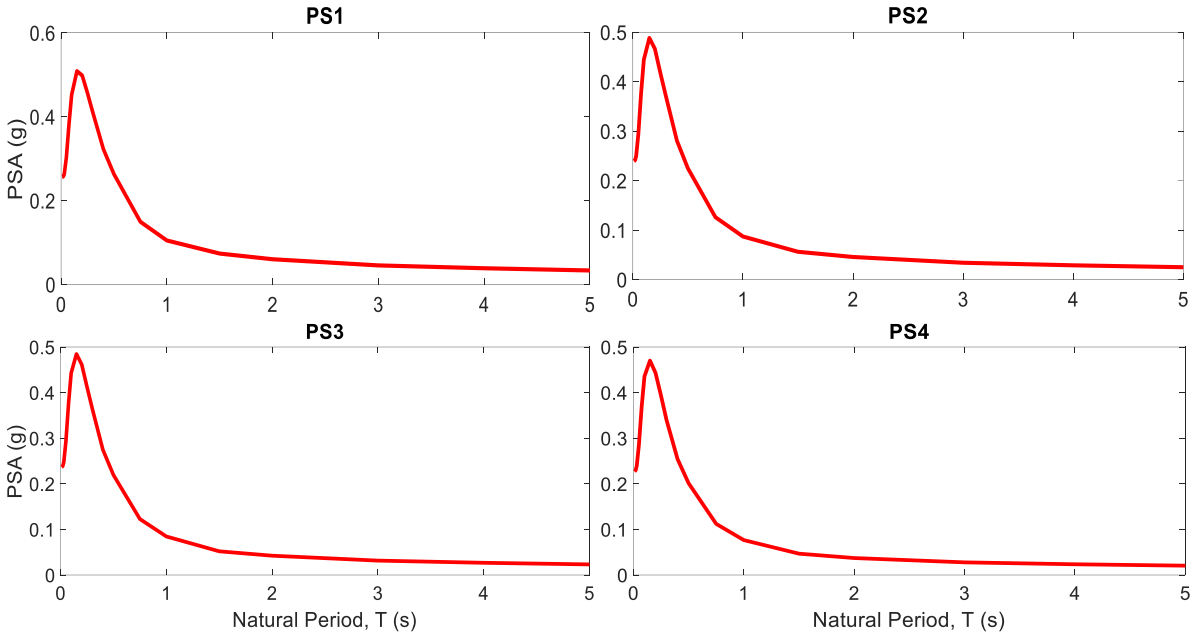

Figure 3.3: *Median Target Response Spectra* (50th percentile) using DSHA method for the four dam locations

3.5.2 84th percentile Target Response Spectra

Ground motion models are formulated to produce the median and one/two standard deviations above/below the mean. The one standard deviation above the median target response spectra is defined as the 84th percentile target response spectra. This is again calculated using the two PEER NGA West2 GMMs. The envelope of the low magnitude earthquake at a shorter distance and high magnitude earthquake at a farther distance for the 84th percentile target response spectra is shown in **Figure 3.4**. This finalized 84th percentile target response spectra is shown in **Figure 3.5**.

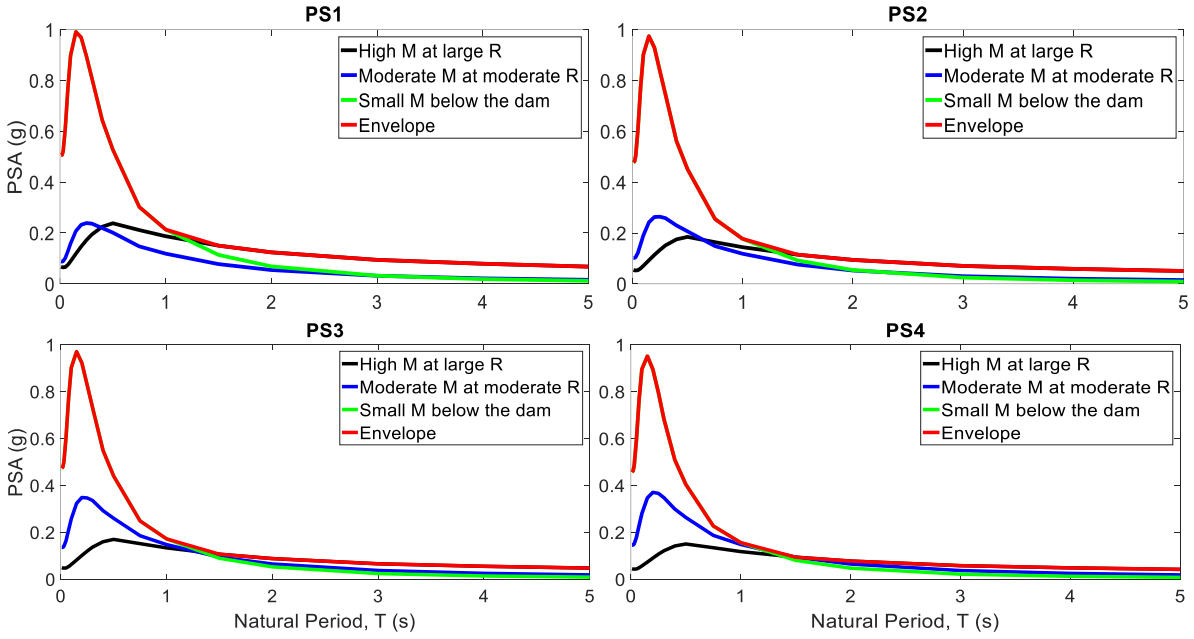

Figure 3.4: Envelope *84th percentile Target Response Spectra* considering critical scenarios for the four dam locations

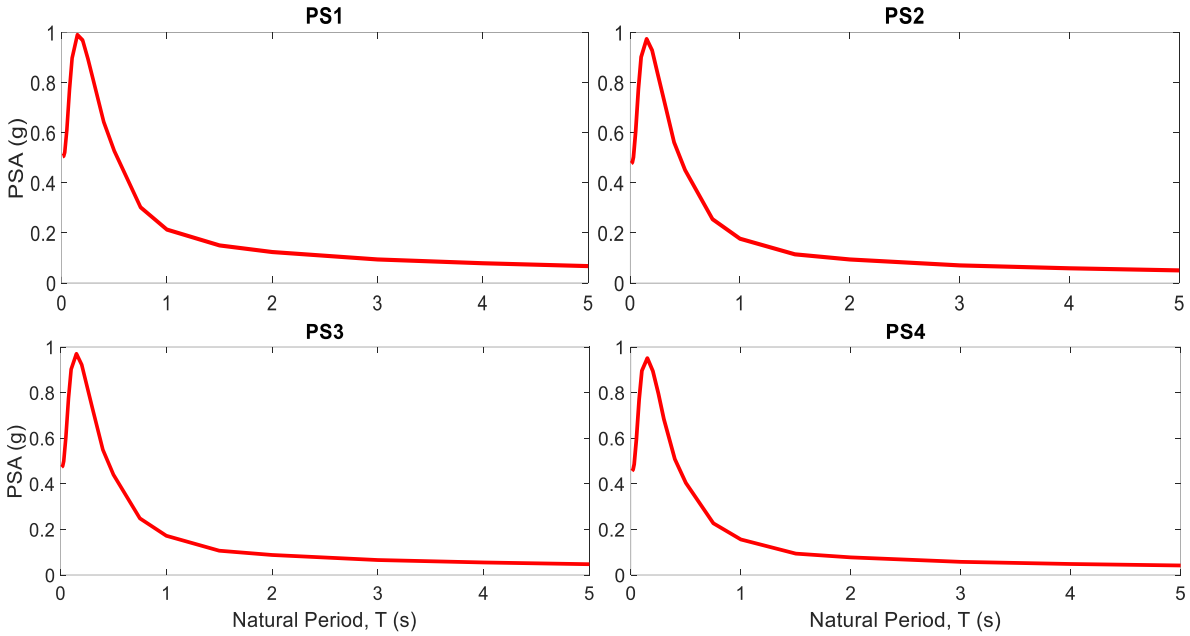

Figure 3.5: *84th percentile Target Response Spectra* using DSHA method for the four dam locations

3.5.3 Design Basis Earthquake (DBE) conditions Target Response Spectra

The one standard deviation below the median target response spectra is defined as the target response spectra for the DBE conditions. This is again calculated using the two PEER NGA West2 GMMs. The envelope of the low magnitude earthquake at a shorter distance and high magnitude earthquake at a farther distance for the DBE target response spectra is shown in **Figure 3.6**.

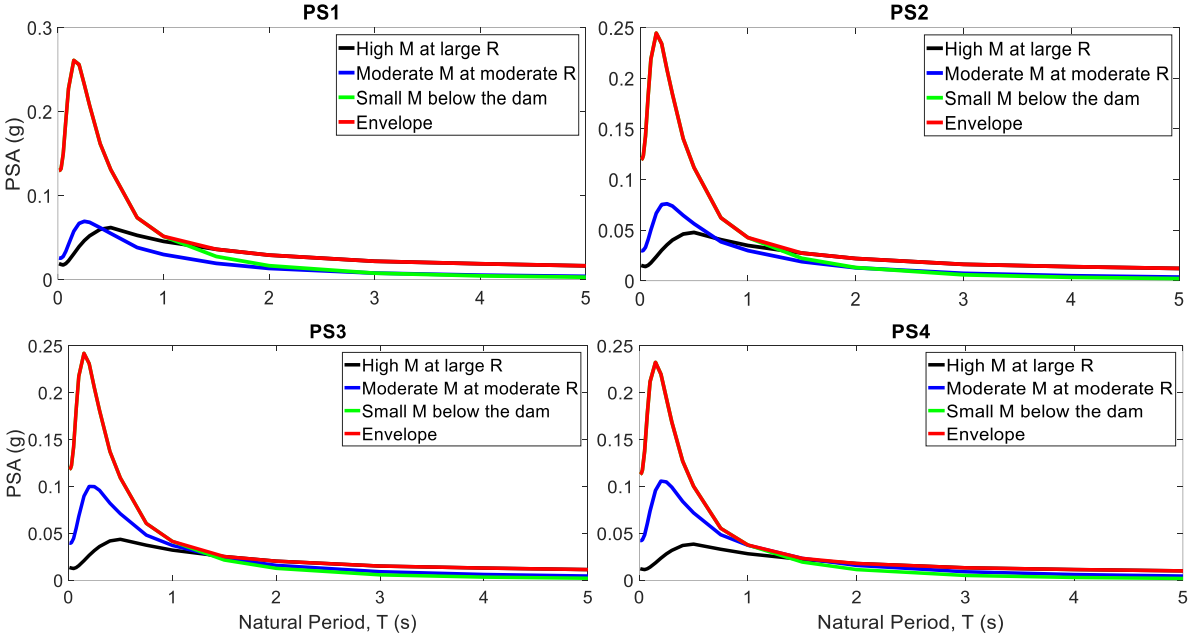

Figure 3.6: *DBE Target Response Spectra* considering critical scenarios for the four dam locations

This finalized DBE target response spectra is shown in **Figure 3.7**.

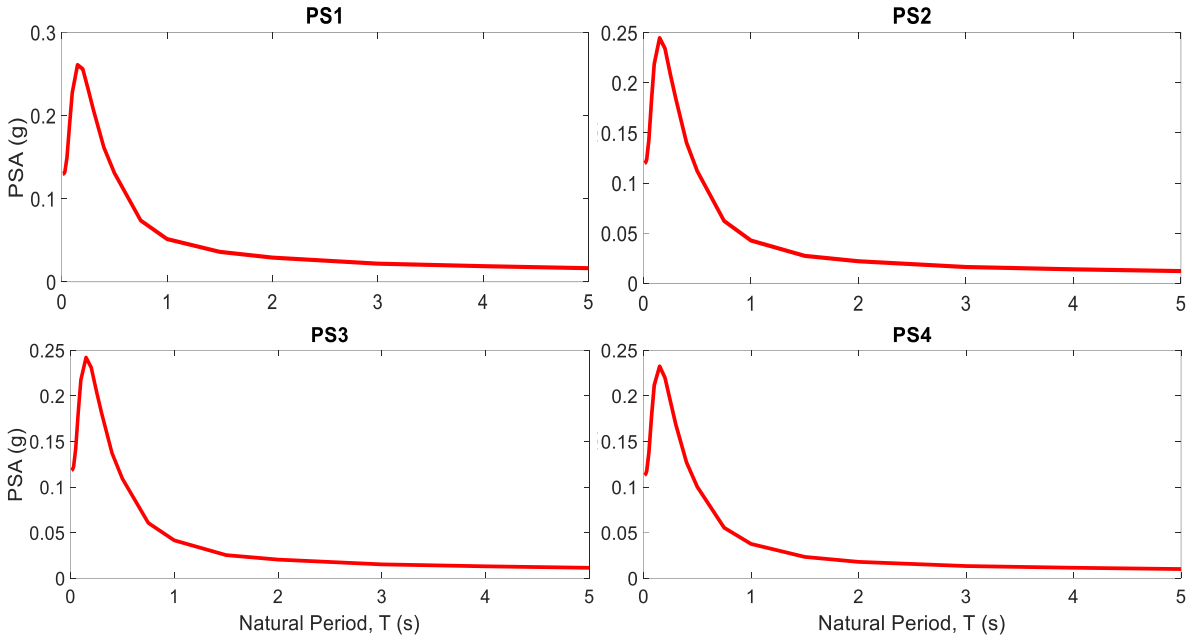

Figure 3.7: *DBE Target Response Spectra* using DSHA method for the four dam locations

Table 3.8 shows the estimated 5%-damped, median, 84th percentile, and DBE horizontal spectral accelerations at PGA, 0.5 second (s) and 1 second (s) using the target response spectra at each of the dam locations from **Figure 3.3, Figure 3.5, and Figure 3.7**.

Table 3.8: *Horizontal Spectral Accelerations* (5%-damped) at selected spectral periods for all the four dam locations

PS-1								
PGA – Acceleration (g)			0.5s – Acceleration (g)			1s – Acceleration (g)		
Median	84th percentile	DBE	Median	84th percentile	DBE	Median	84th percentile	DBE
0.255	0.501	0.129	0.263	0.528	0.131	0.105	0.213	0.051
PS-2								
PGA – Acceleration (g)			0.5s – Acceleration (g)			1s – Acceleration (g)		
Median	84th percentile	DBE	Median	84th percentile	DBE	Median	84th percentile	DBE
0.238	0.474	0.119	0.225	0.451	0.112	0.087	0.177	0.043
PS-3								
PGA – Acceleration (g)			0.5s – Acceleration (g)			1s – Acceleration (g)		
Median	84th percentile	DBE	Median	84th percentile	DBE	Median	84th percentile	DBE
0.235	0.470	0.118	0.219	0.440	0.109	0.084	0.172	0.042
PS-4								
PGA – Acceleration (g)			0.5s – Acceleration (g)			1s – Acceleration (g)		
Median	84th percentile	DBE	Median	84th percentile	DBE	Median	84th percentile	DBE
0.226	0.453	0.112	0.201	0.404	0.100	0.077	0.156	0.038

4.
Probabilistic Seismic Hazard Assessment

4.1 INTRODUCTION

This section describes the major inputs to the site-specific *Probabilistic Seismic Hazard Analysis (PSHA)*. It includes developing probabilistic estimates of the earthquake ground motions at the dam site, including summary results and a comparison with earthquake ground motions developed from the DSHA.

PSHA is used to estimate the likelihood that a specified earthquake ground motion will be exceeded during a specified time period. The likelihood of exceedance is determined based on the probability of occurrence of any earthquake of with a range of magnitudes typically within about 500 km of a site, and the rate at which ground motions attenuate while traveling from the source to the site. PSHA accounts for both aleatory variability and epistemic uncertainty. Aleatory variability describes the natural randomness of the earthquake process, and epistemic uncertainty is the degree to which a scientific model differs from the natural process it represents.

Epistemic uncertainty usually occurs because of limited data or knowledge about the natural process. One of the main advantages of PSHA is that both aleatory variability and epistemic uncertainties can be quantified and incorporated. The PSHA method used for this study generally follows the Cornell-McGuire framework (Cornell 1968; McGuire 1976, 2004).

4.2 GROUND MOTION MODELS (ATTENUATION RELATIONS)

Site locations, site ground conditions, and GMMs used in the PSHA calculations are taken as the identical values which were used in the DSHA calculations (**Section 3.2** and **Section 3.4**). The two NGA West2 GMMs – Abrahamson et al. (2014) and Boore et al. (2014) were weighted equally (i.e., 0.50 each) while being used here.

4.3 TARGET RESPONSE SPECTRA

As against the deterministic target spectrum based on a single earthquake magnitude and distance scenario, the PSHA approach considers all the magnitude and distance pairs with their expected recurrence rates based on the past seismicity.

The probabilistic target spectrum is defined with a specified confidence level (probability of not exceeding) during a given period of exposure, or equivalently the return period. As per the NCSDP guidelines, MCE level of probabilistic target spectrum is defined for confidence level of 0.98 in 50 years, which is equivalent to return period of about 2475 years. On the other hand, DBE level of probabilistic target spectrum is defined for confidence level of 0.90 in 50 years or return period of 475 years.

The PSHA formulation for spectral acceleration $S_A(T)$ at natural period of T second is based on the following cumulative probability distribution function (McGuire, 2004; Gupta, 2009, 2013)

$$P[S_A(T)] = exp\{-Y \sum_{n,i,j} q_n\,[SA(T)|M_j, R_{ij}] \cdot \upsilon_{ni}(M_j)\} \qquad \textbf{(4.1)}$$

In this expression, Y is the exposure period (taken as 50 years) and $\upsilon_{ni}(M_j)$ is the annual occurrence rate of earthquakes within a small magnitude interval with central magnitude M_j at the ith epicentral location in the nth seismic source zone. The quantity $q[S_A(T)|M_j, R_{ij}]$ is the probability of exceeding the spectral amplitude $S_A(T)$ due to magnitude M_j at source to site distance R_{ij} associated with this magnitude occurring at the ith epicentral location.

The probability $q[SA(T)|M_j, R_{ij}]$ is obtained as the complementary of the probability defined by eqn. (4.1) by using the mean and standard deviation values estimated using GMMs of Abrahamson and Silva (2008).

The $n(M_j)$ is then distributed suitably among a grid of small size cells covering the entire source zone area. Assuming that for the periods of interest in engineering applications the future seismicity will broadly follow the spatial pattern of the past seismicity without any radical change, the spatially averaged epicentral density of past earthquakes is used to distribute the rate $n(M_j)$ for each source zone (Gupta, 2013) to get the desired occurrence rate $\upsilon_{ni}(M_j)$.

Using the occurrence rates $\upsilon_{ni}(M_j)$ and the probabilities $q_n[PSA(T)|M_j, R_{ij}]$ estimated as above, the probability distribution function is computed to obtain the 5 % damped horizontal response spectra with confidence levels of 0.98 and 0.90 and exposure period Y=50 years.

The MCE and DBE levels of target response spectra using PSHA method are shown in **Figure 4.1** and **Figure 4.2** respectively.

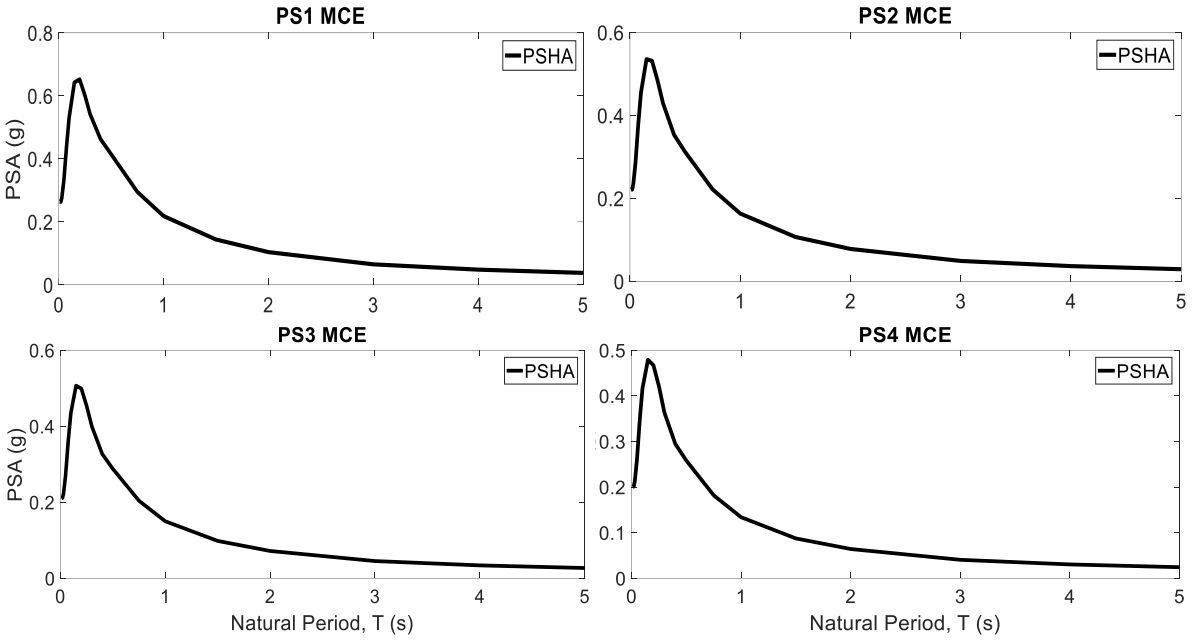

Figure 4.1: *MCE Target Response Spectra* using *PSHA* method for the four dam locations

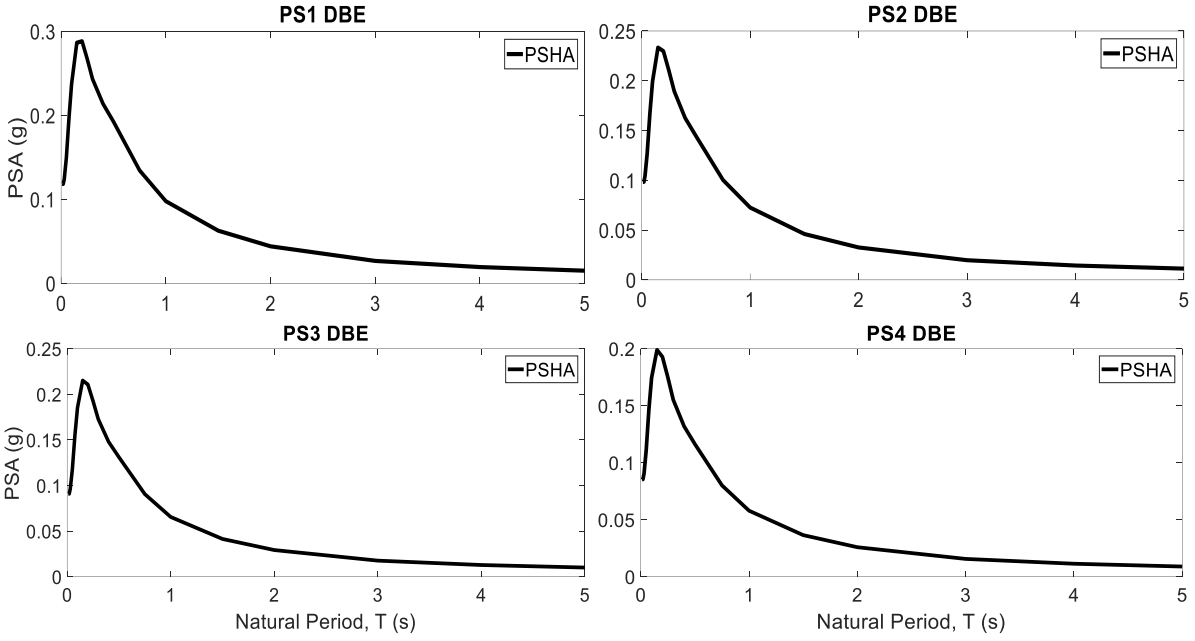

Figure 4.2: *DBE Target Response Spectra* using *PSHA* method for the four dam locations

4.4 COMPARISON OF PSHA AND DSHA

The PSHA and DSHA results are compared in **Figures 4.3** and **4.4** for MCE and DBE conditions respectively. As per the NCSDP guidelines, if the results of PSHA and DSHA differ by 25% or less, the final MCE and DBE target spectrum is taken as the envelope of the deterministic and the probabilistic spectra.

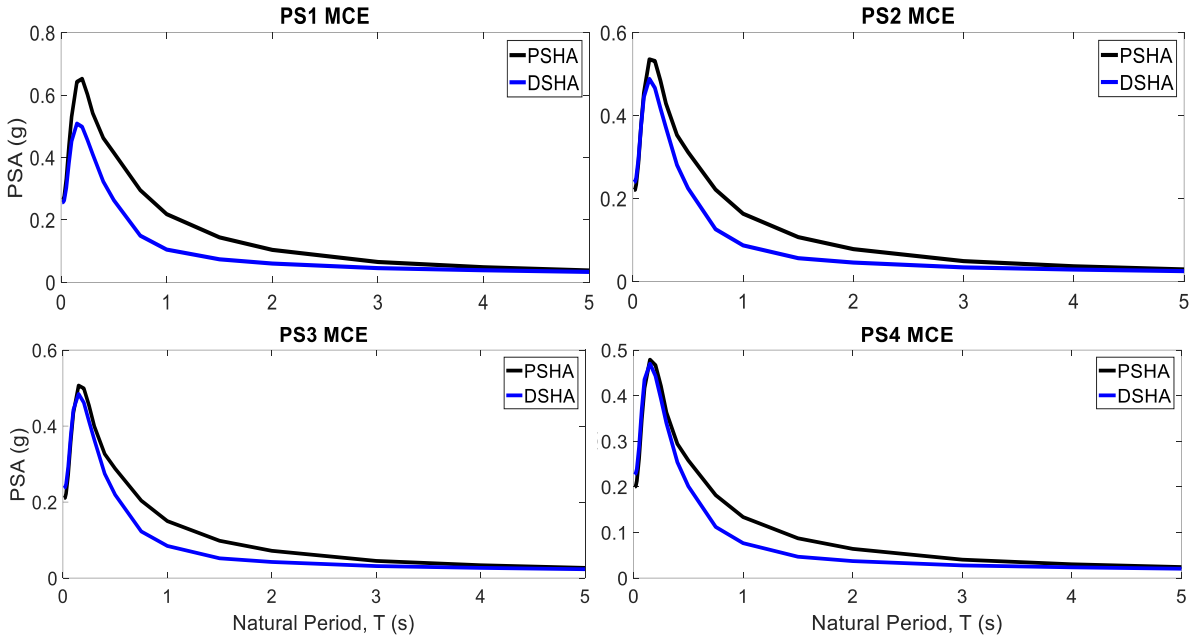

Figure 4.3: Comparison of *MCE Target Response Spectra* using *PSHA* and *DSHA* method for the four dam locations

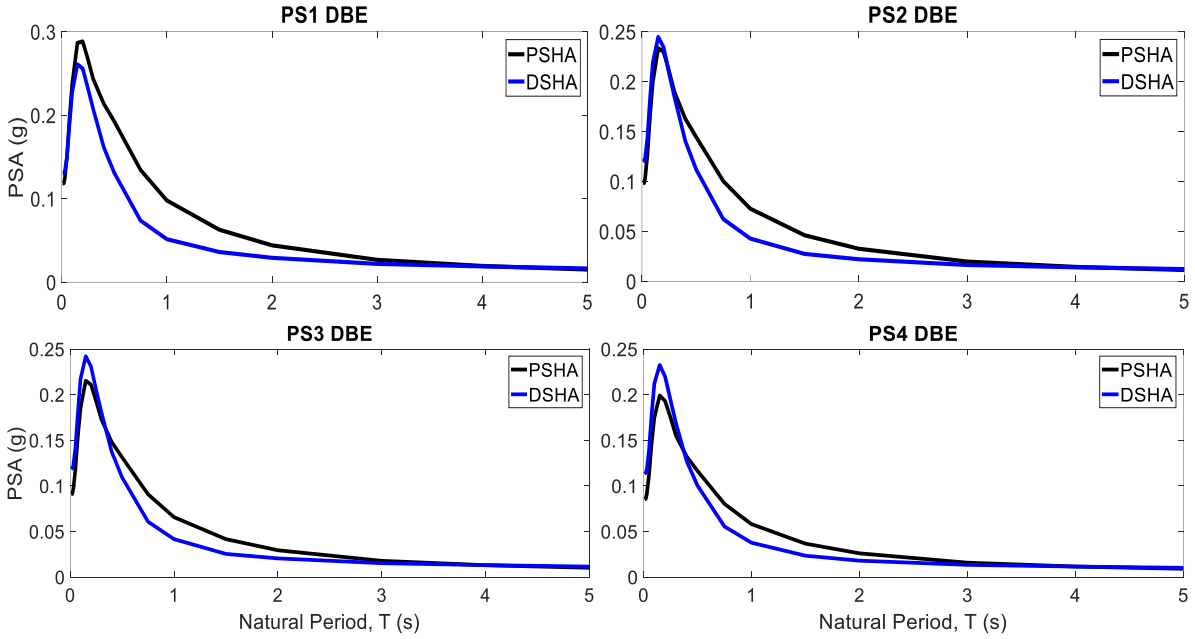

Figure 4.4: Comparison of *DBE Target Response Spectra* using *PSHA* and *DSHA* method for the four dam locations

The final target envelope spectrum for MCE and DBE conditions developed using the envelope of *PSHA* and *DSHA* Spectra is shown in **Figure 4.5** and **Figure 4.6** respectively.

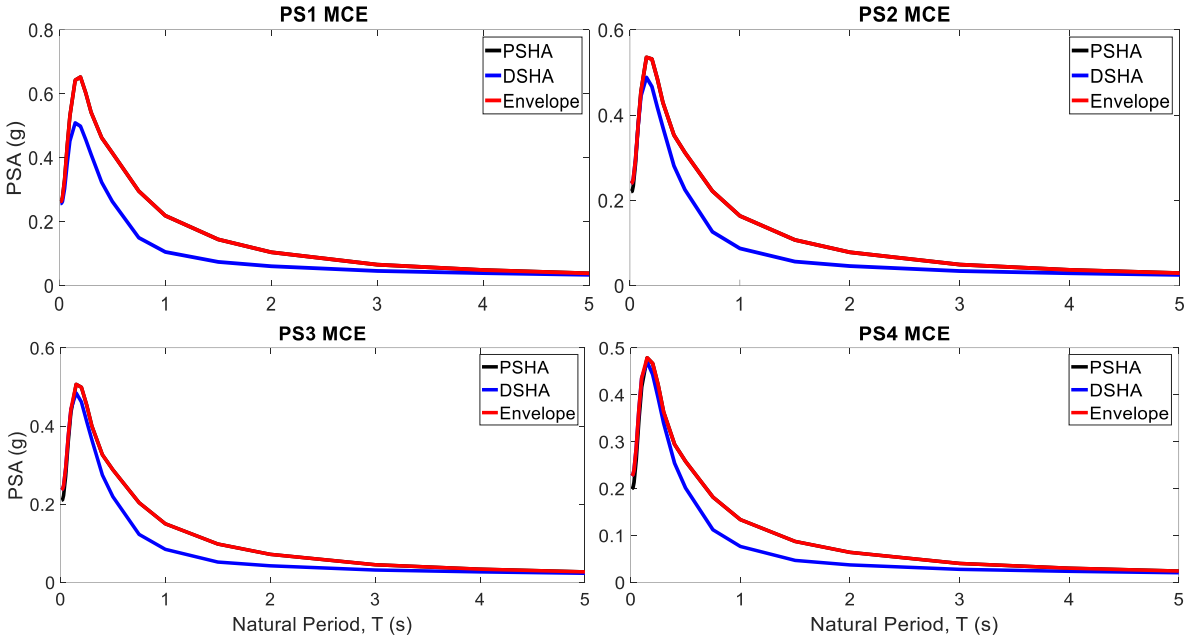

Figure 4.5: Final *MCE Target Response Spectra* for the four dam locations

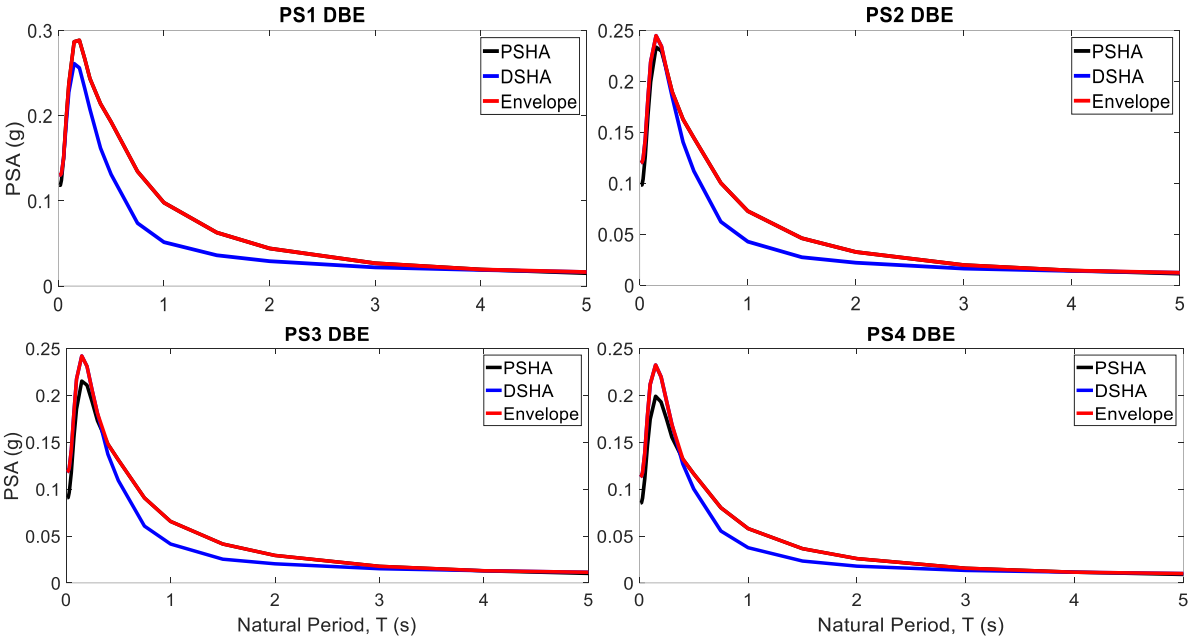

Figure 4.6: Final *DBE Target Response Spectra* for the four dam locations

4.5 EARTHQUAKE ACCELERATION TIME HISTORIES AND RESPONSE SPECTRA

Design accelerograms compatible with the 5% damped target spectra developed in the last section for both the horizontal and vertical components of motion are generated independently, such that the horizontal and vertical accelerograms are uncorrelated. This is done for both the MCE and DBE conditions. This is done by using an amplitude modulated Gaussian white-noise as the initial

accelerogram, which is matched with the target spectrum using an iterative process as explained in Gupta and Joshi (1993). The strong-motion stationary duration of the simulated accelerograms has been obtained from the frequency-dependent scaling relationships (Novikova and Trifunac, 1994) as 7s.

Baseline correction (Boore and Bommer, 2005) is applied to the accelerograms to get realistic velocity and displacement curves by integration of the accelerograms. The design accelerograms are then used to compute smoothened design response spectra for six different damping values of 2%, 3%, 5%, 7%, 10%, and 15 % of critical.

The design accelerograms for the DBE and MCE conditions are shown for each of the dam locations from **Figure 4.7** through **Figure 4.14.**

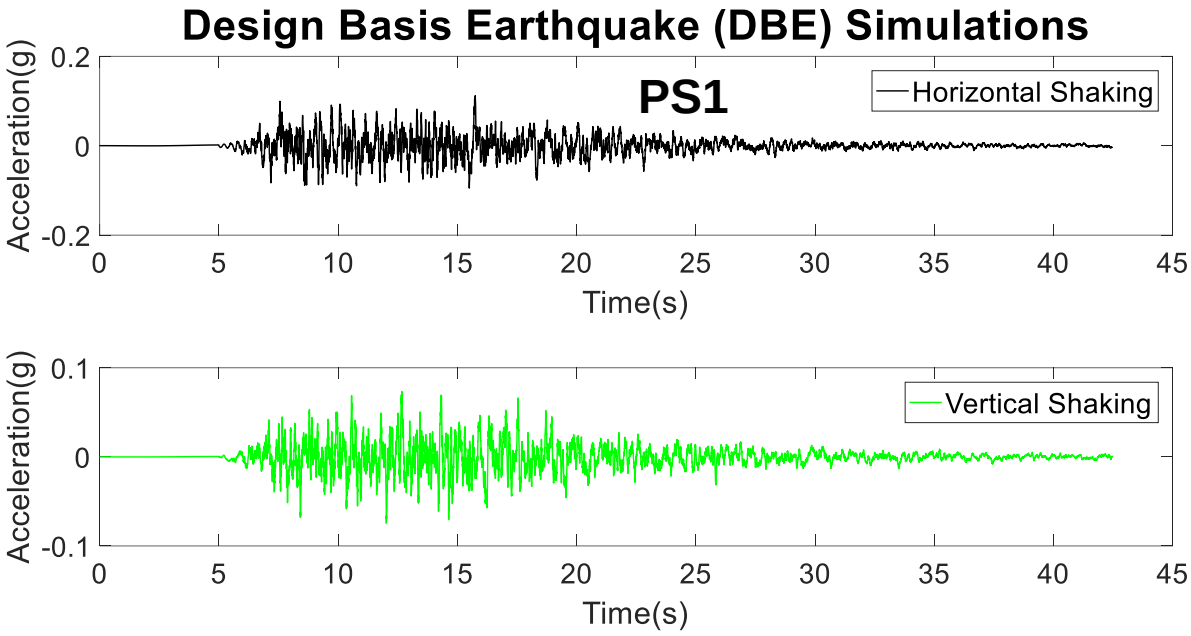

Figure 4.7: *Design Accelerograms* for *DBE* conditions at PS1

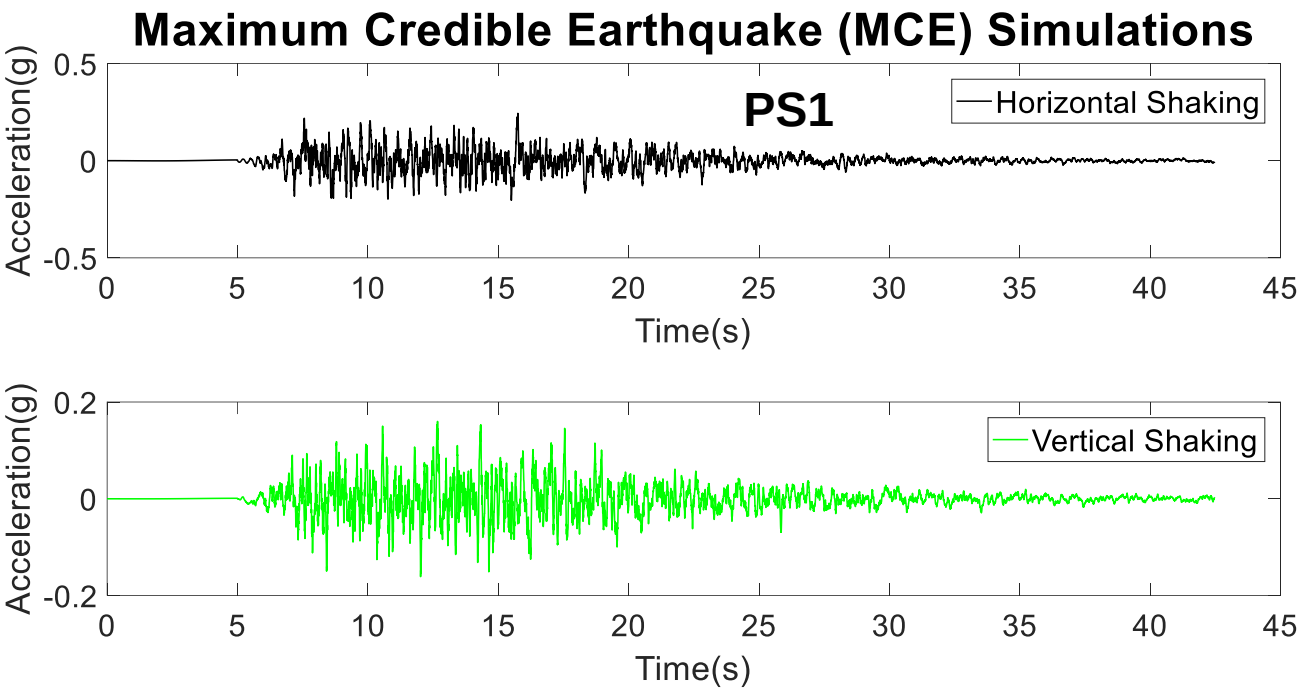

Figure 4.8: *Design Accelerograms* for *MCE* conditions at PS1

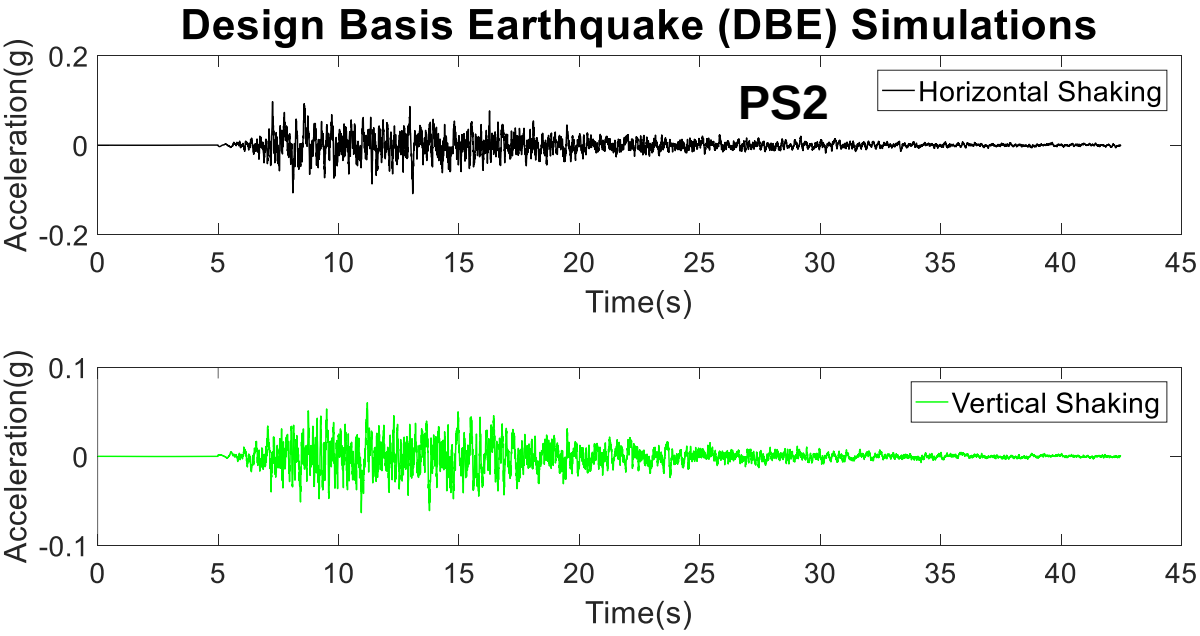

Figure 4.9: *Design Accelerograms* for *DBE* conditions at PS2

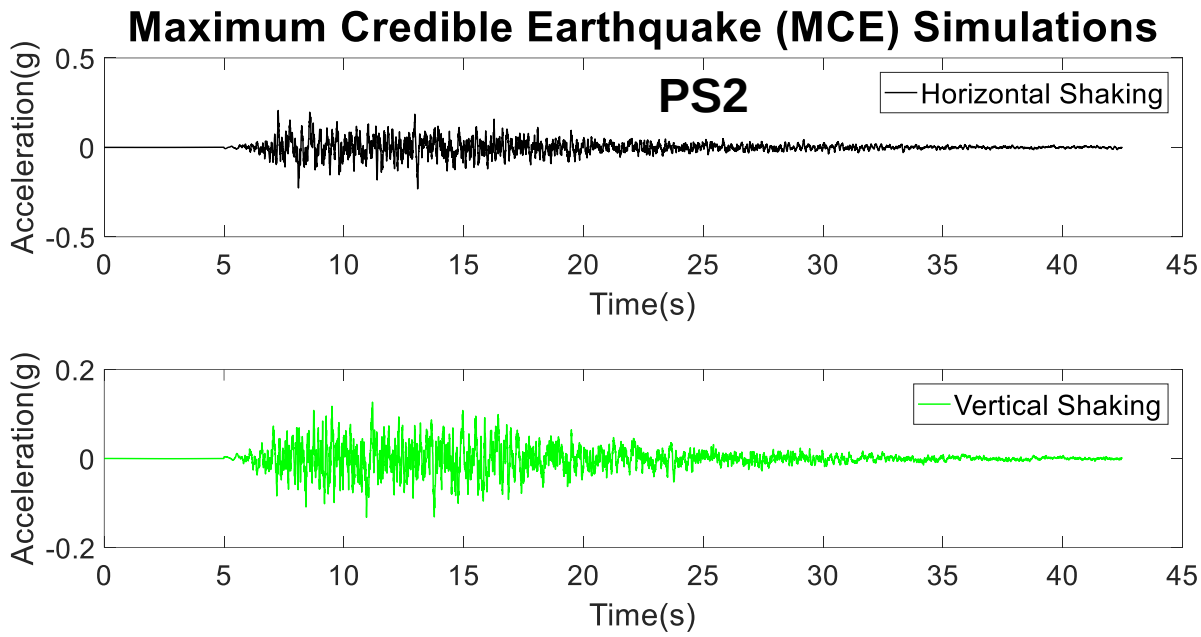

Figure 4.10: *Design Accelerograms* for *MCE* conditions at PS2

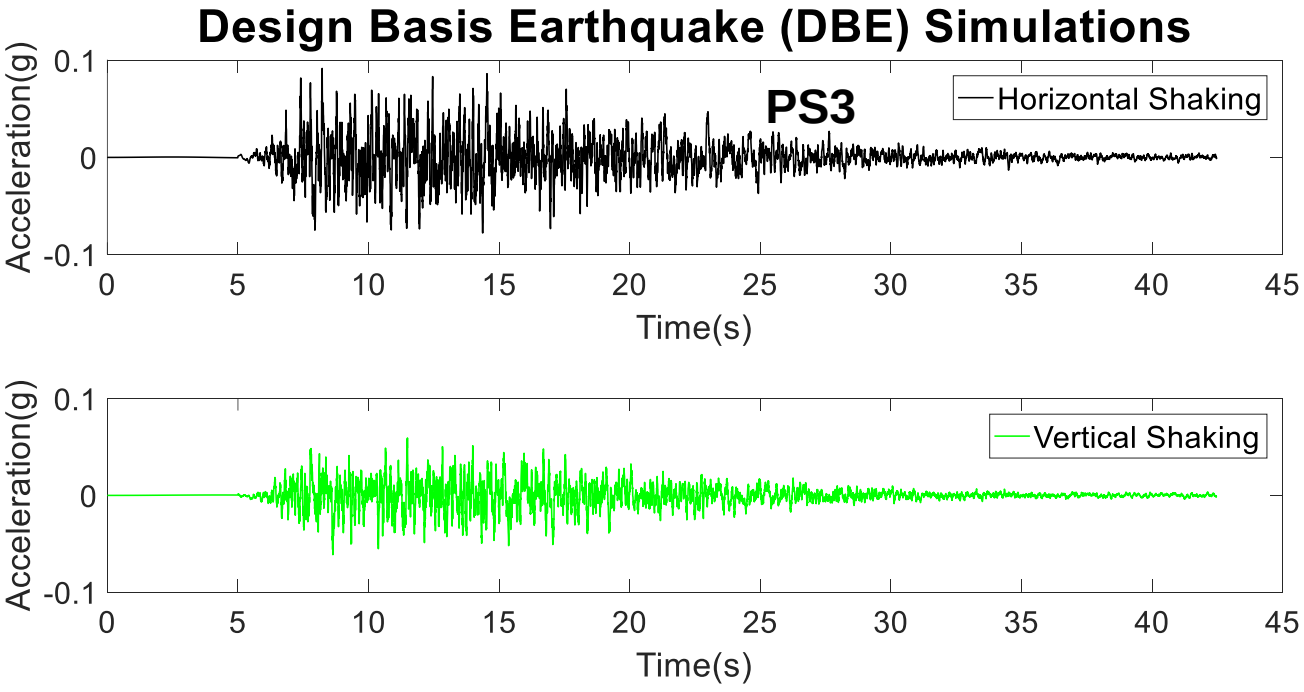

Figure 4.11: *Design Accelerograms* for *DBE* conditions at PS3

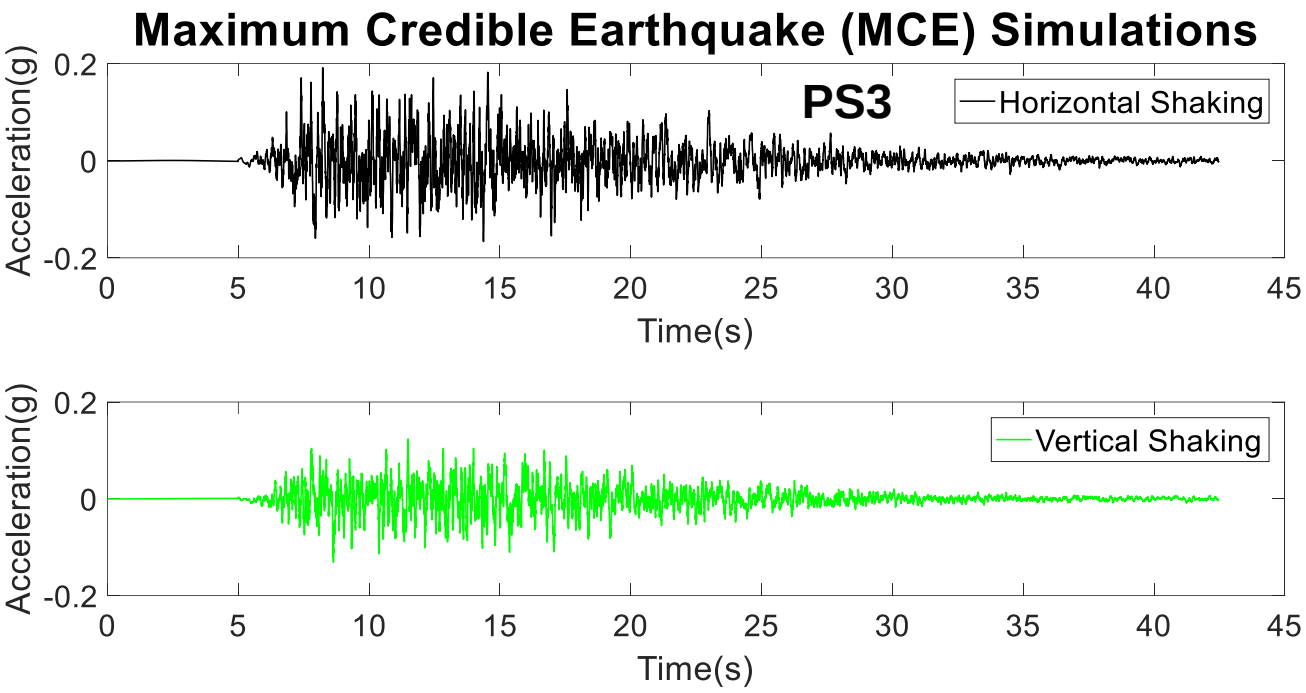

Figure 4.12: *Design Accelerograms* for *MCE* conditions at PS3

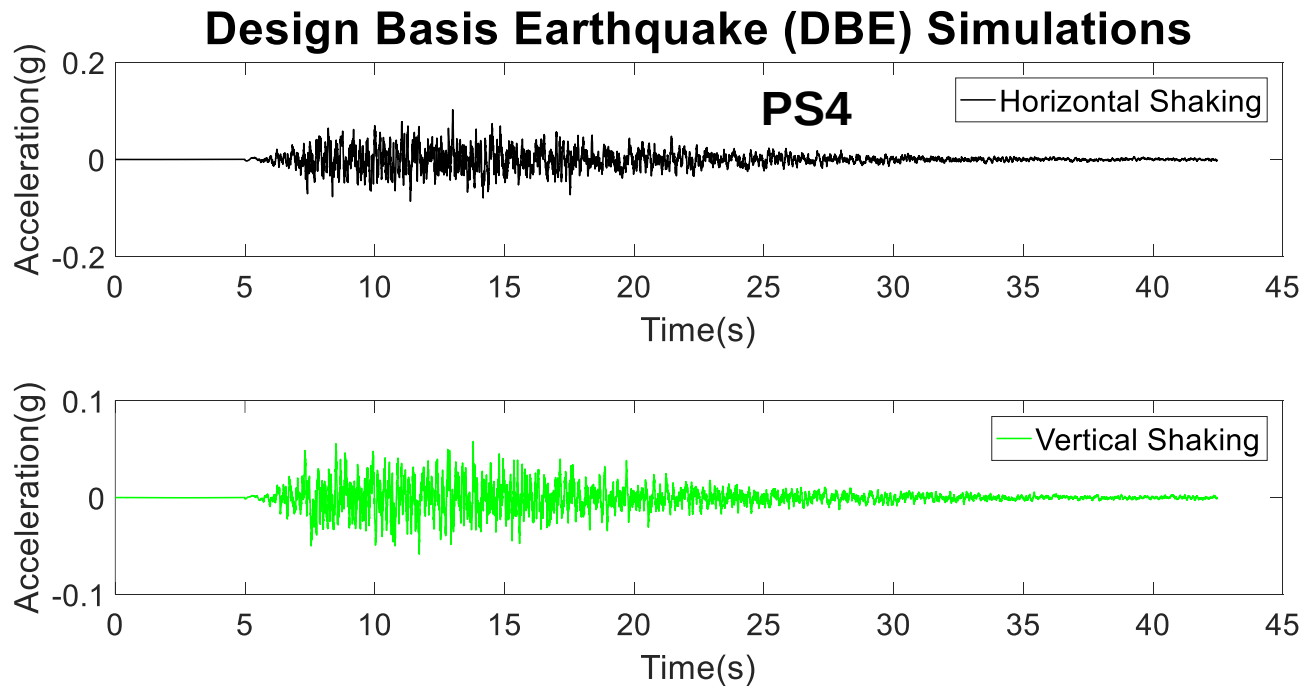

Figure 4.13: *Design Accelerograms* for *DBE* conditions at PS4

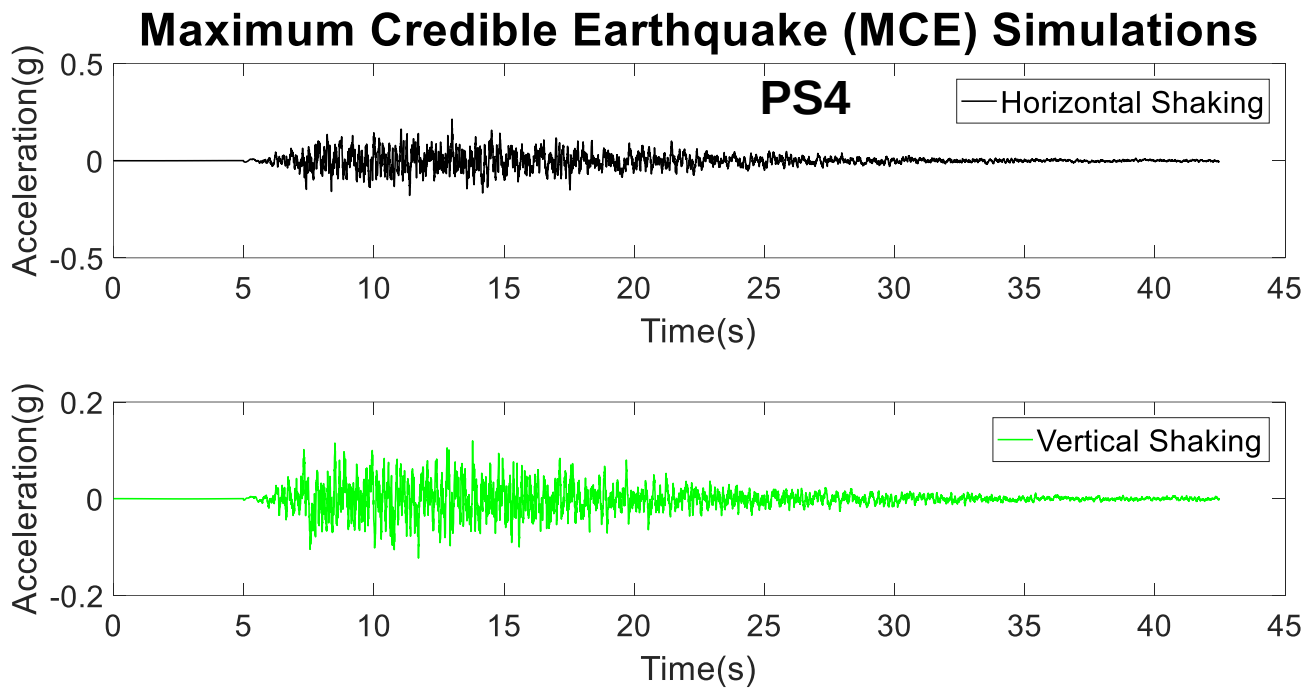

Figure 4.14: *Design Accelerograms* for *MCE* conditions at PS4

The smoothened design spectra for *Horizontal* shaking and *Vertical* shaking of all the four dam locations are shown from **Figure 4.15** through **Figure 4.30** . These are drawn for both DBE and MCE conditions.

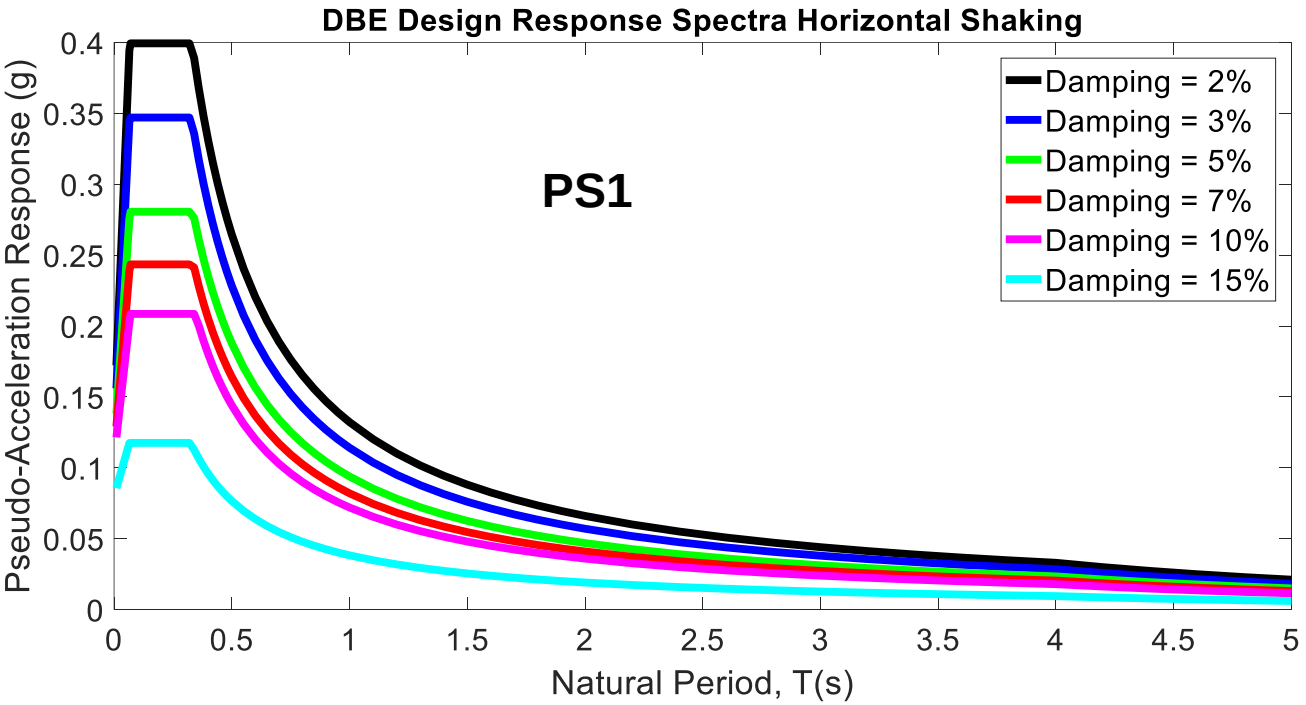

Figure 4.15: *DBE Design Response Spectra* for *Horizontal* shaking at PS1

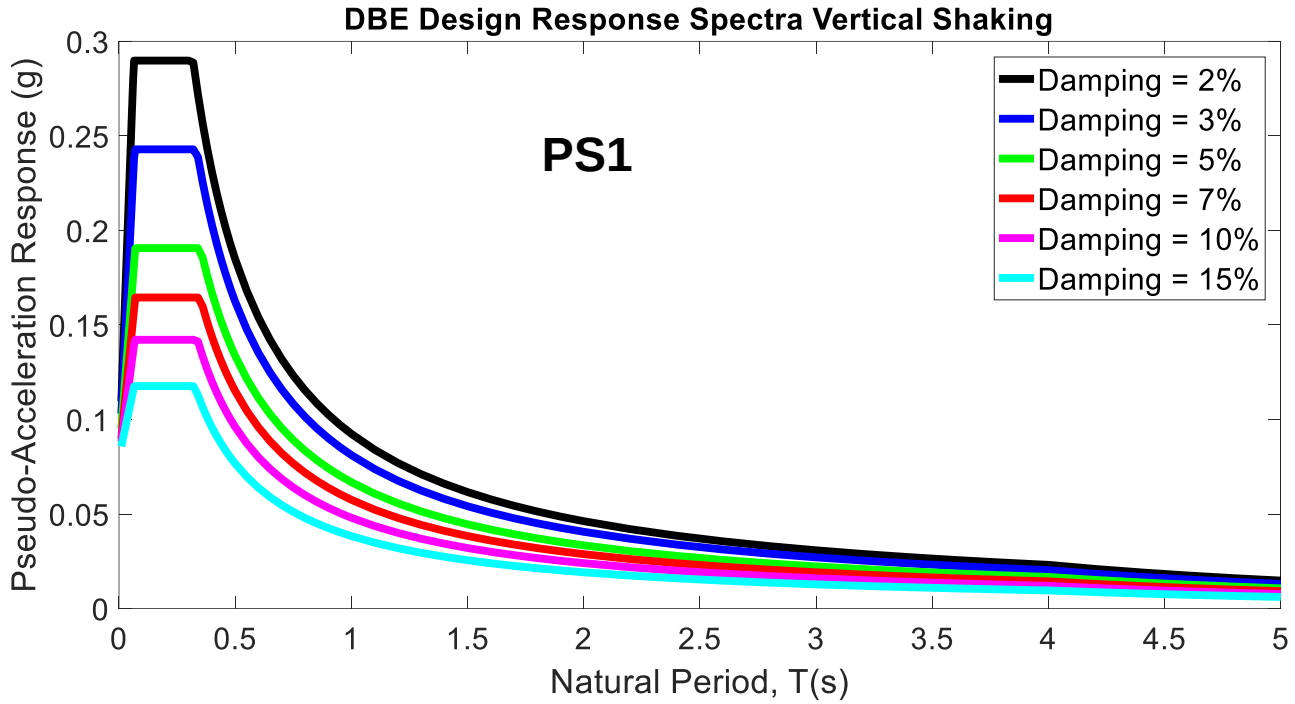

Figure 4.16: *DBE Design Response Spectra* for *Vertical* shaking at PS1

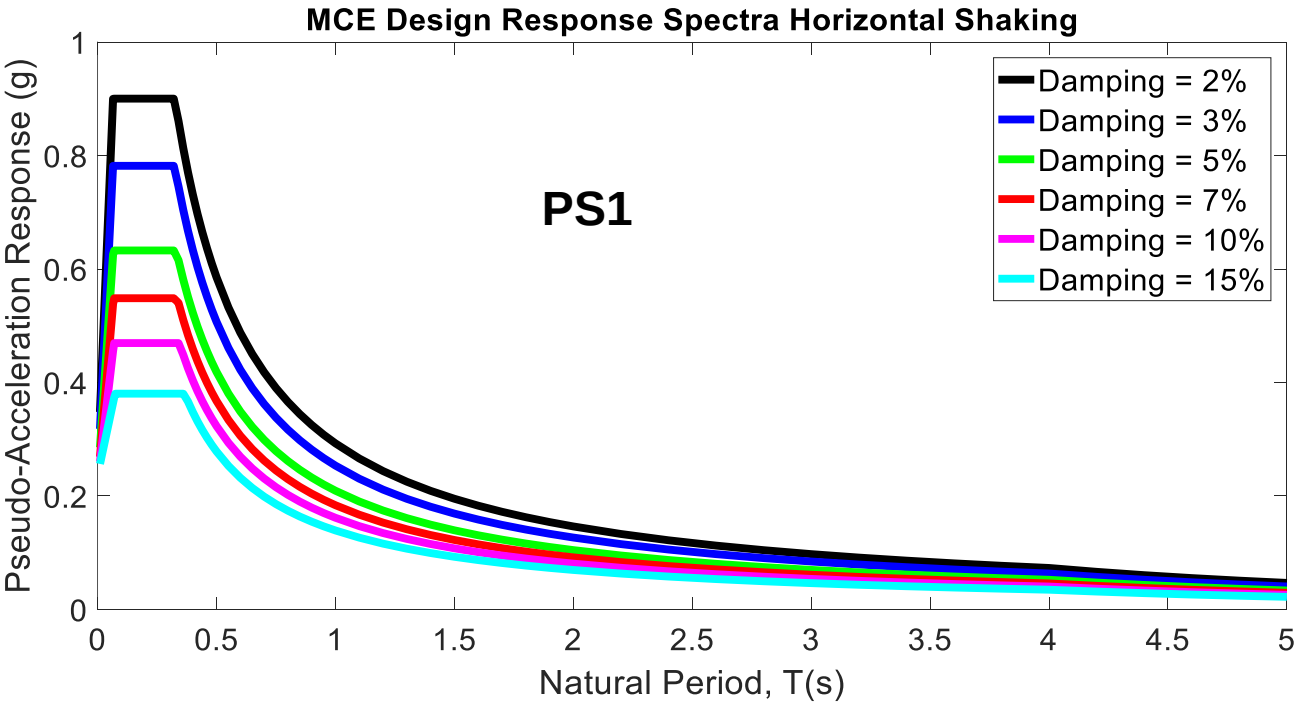

Figure 4.17: *MCE Design Response Spectra* for *Horizontal* shaking at PS1

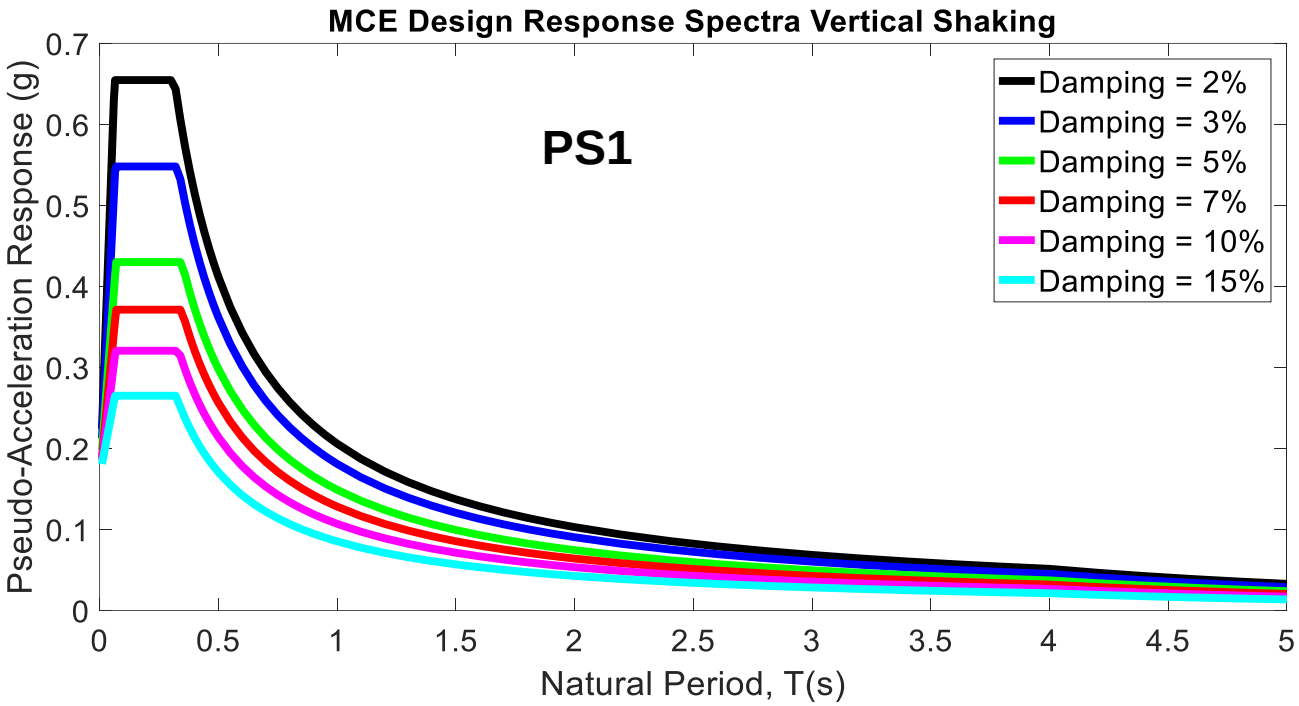

Figure 4.18: *MCE Design Response Spectra* for *Vertical* shaking at PS1

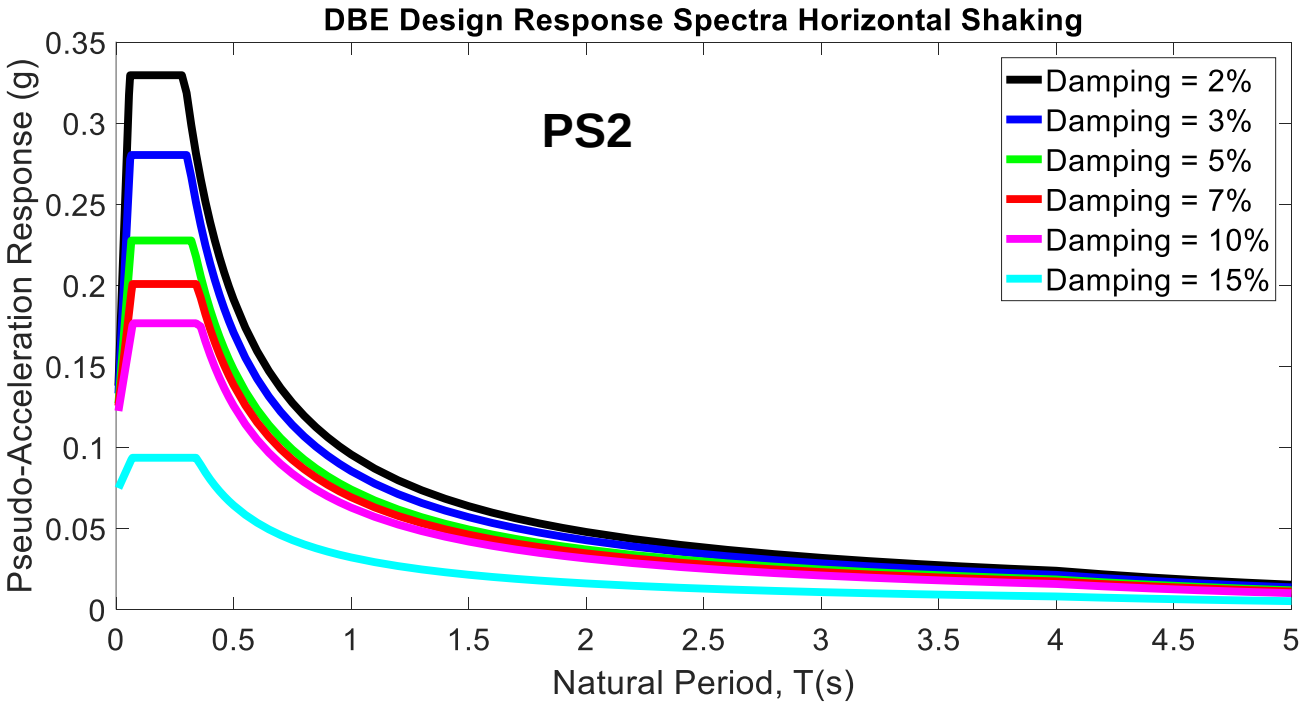

Figure 4.19: *DBE Design Response Spectra* for *Horizontal* shaking at PS2

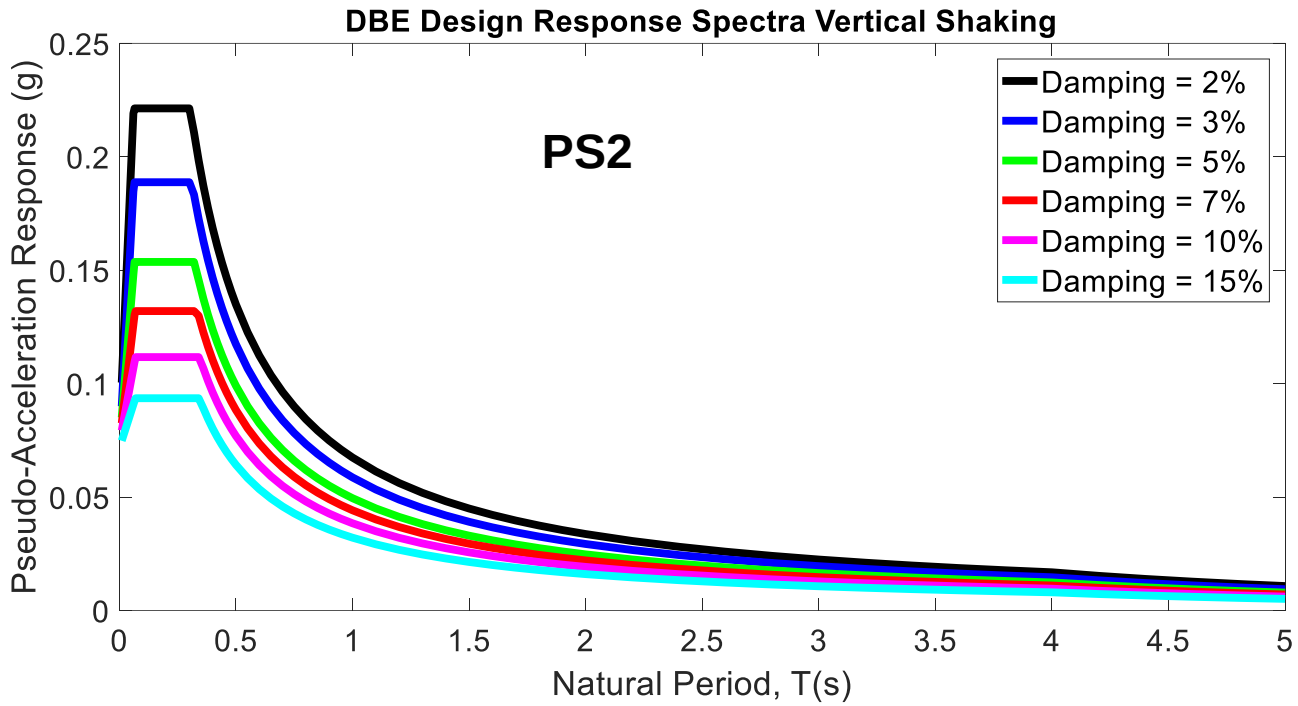

Figure 4.20: *DBE Design Response Spectra* for *Vertical* shaking at PS2

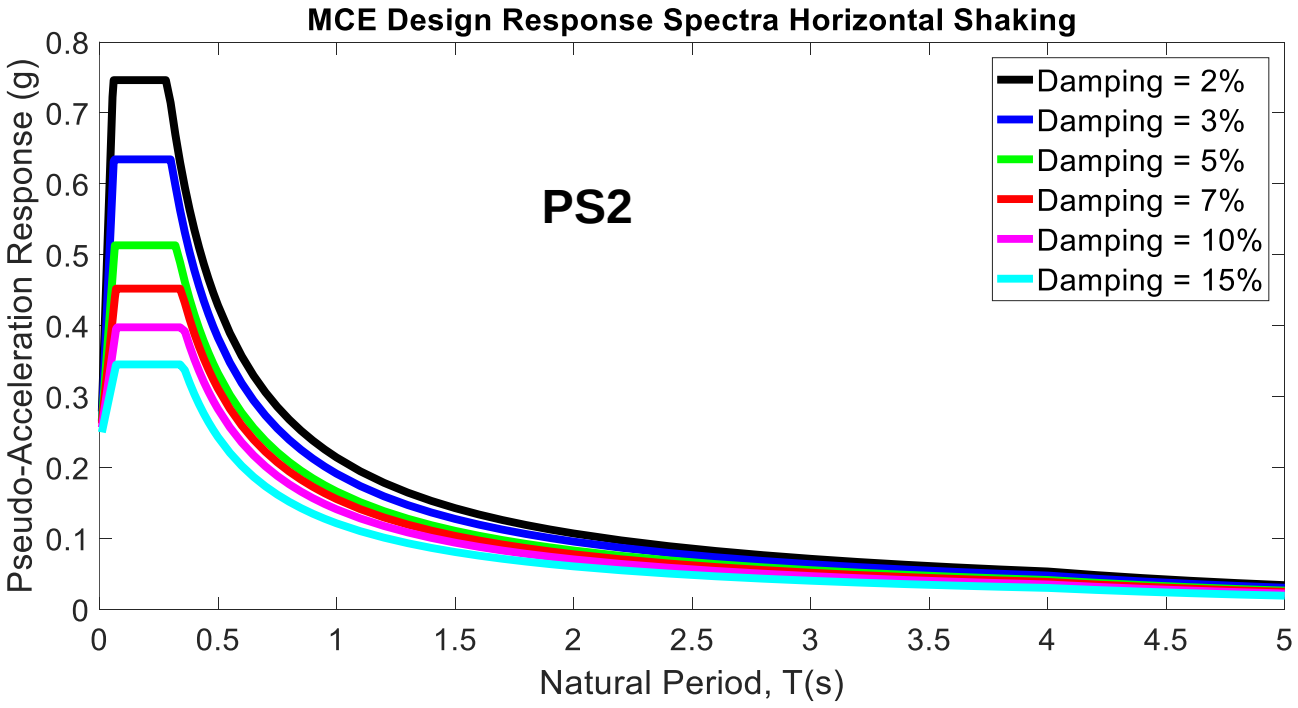

Figure 4.21: *MCE Design Response Spectra* for *Horizontal* shaking at PS2

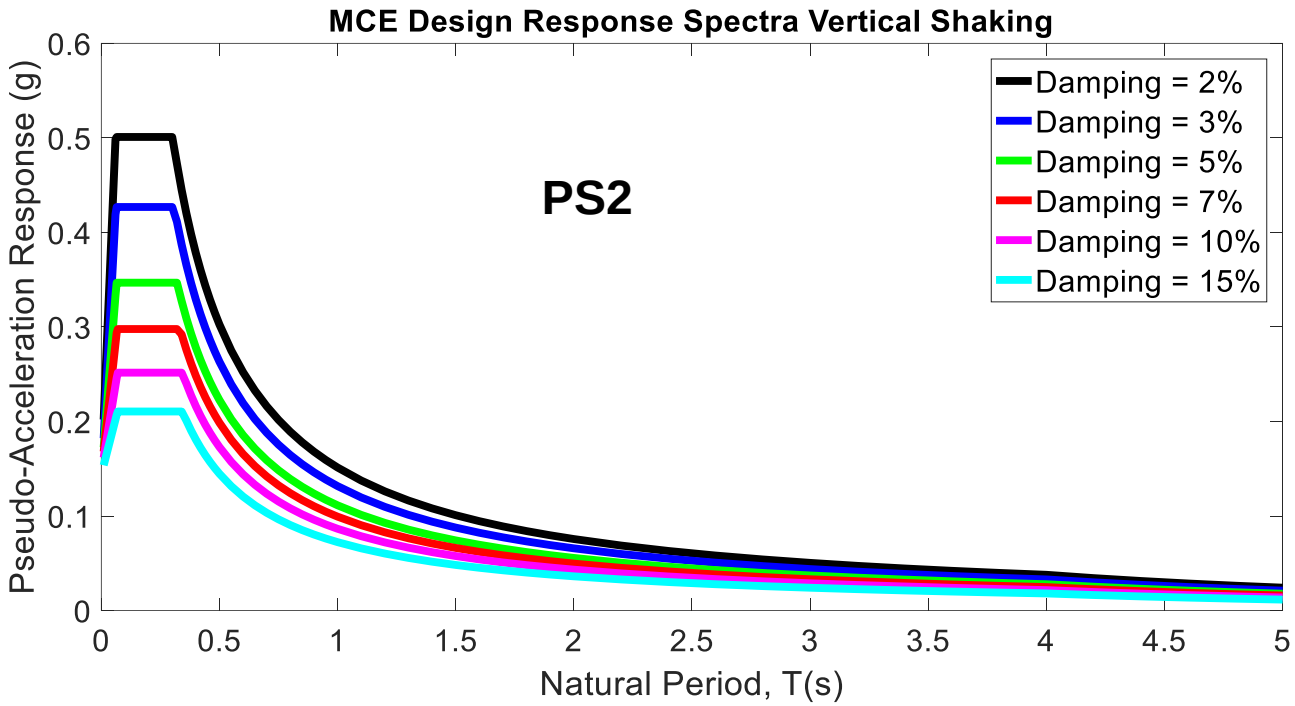

Figure 4.22: *MCE Design Response Spectra* for *Vertical* shaking at PS2

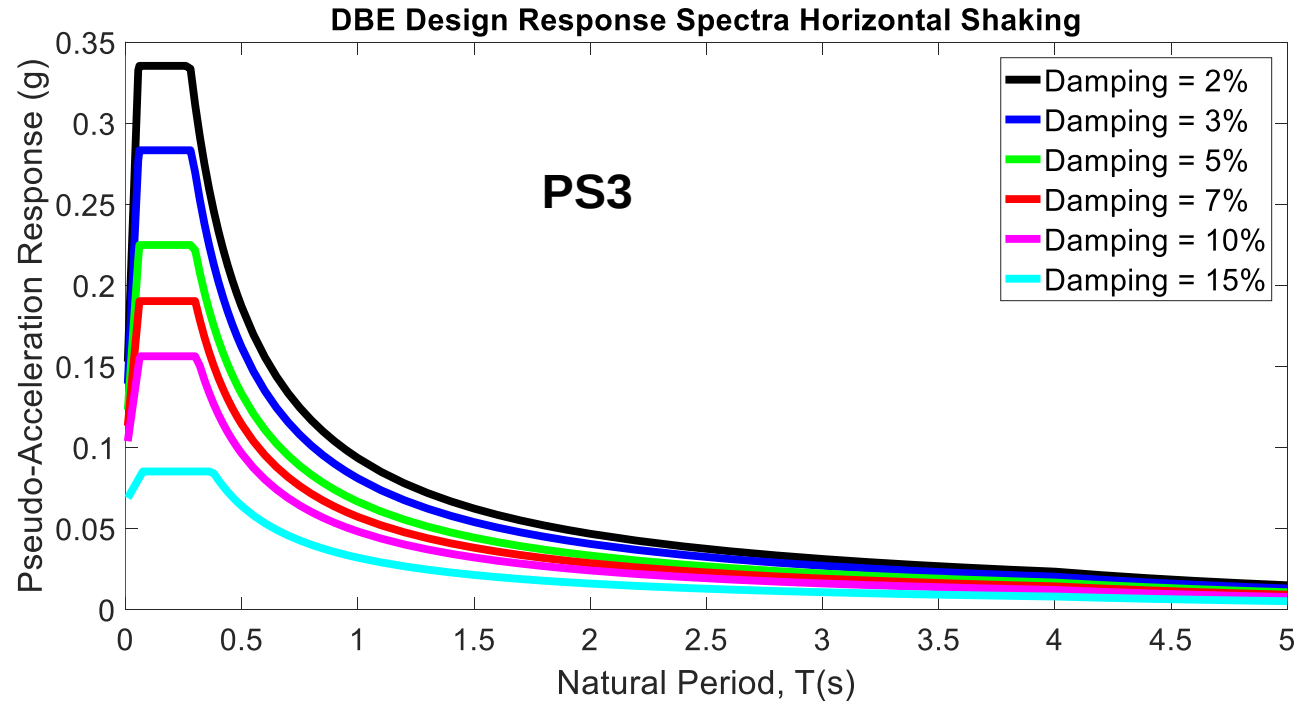

Figure 4.23: *DBE Design Response Spectra* for *Horizontal* shaking at PS3

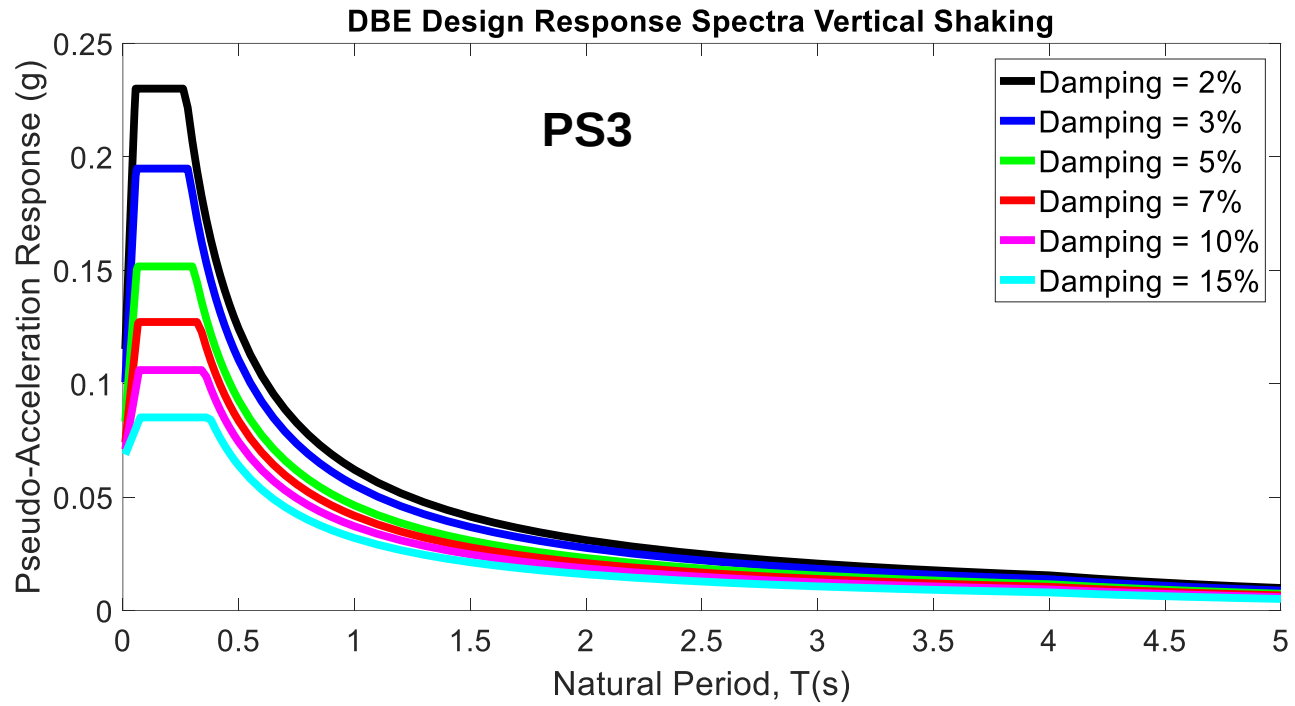

Figure 4.24: *DBE Design Response Spectra* for *Vertical* shaking at PS3

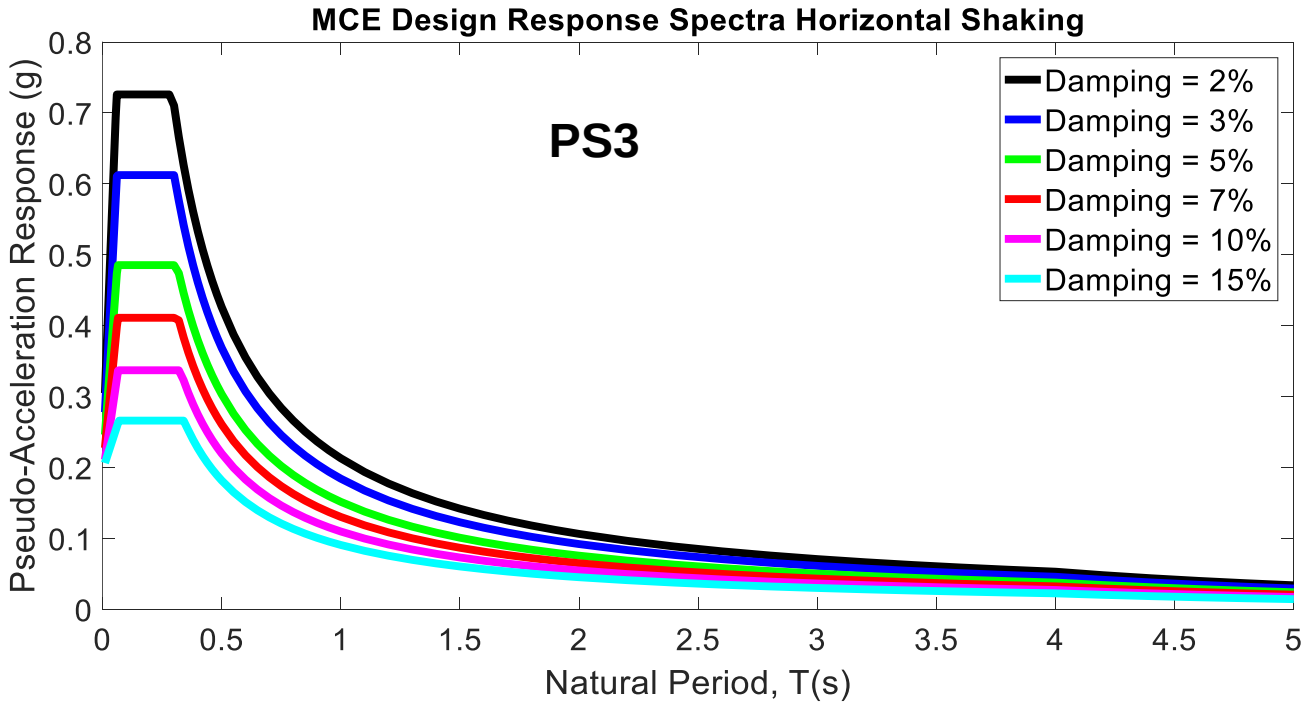

Figure 4.25: *MCE Design Response Spectra* for *Horizontal* shaking at PS3

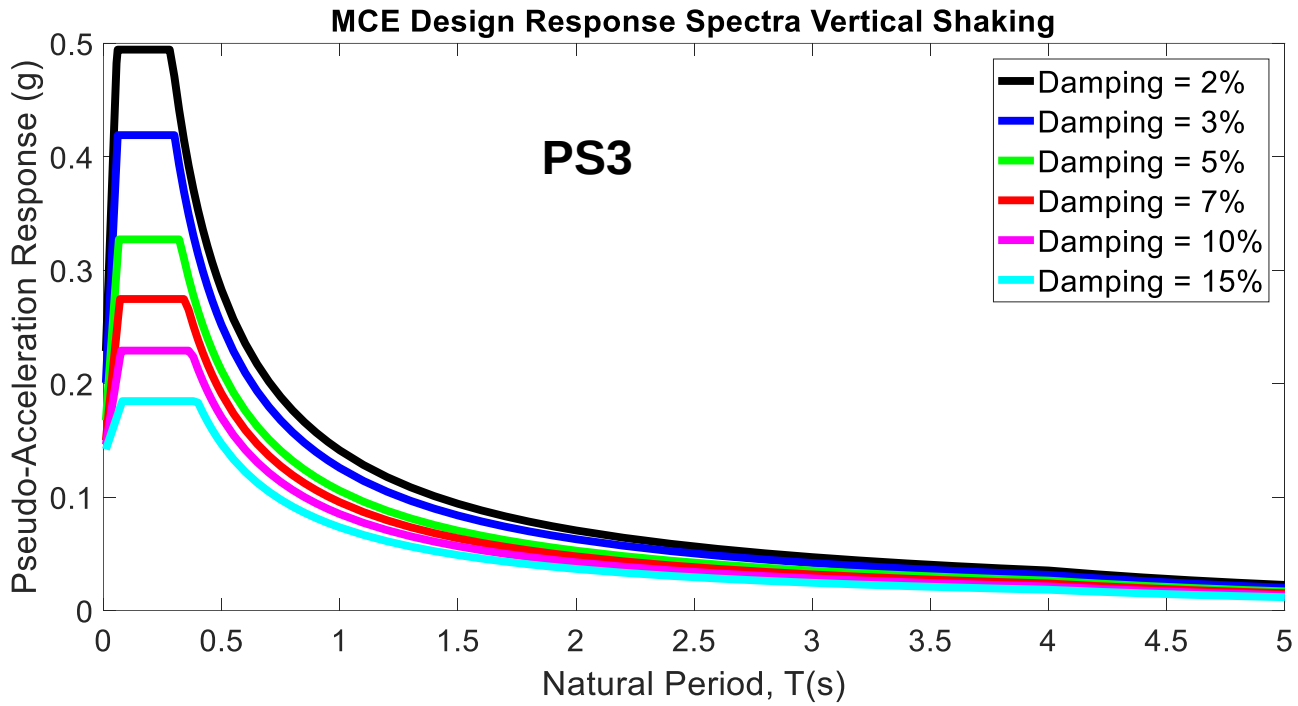

Figure 4.26: *MCE Design Response Spectra* for *Vertical* shaking at PS3

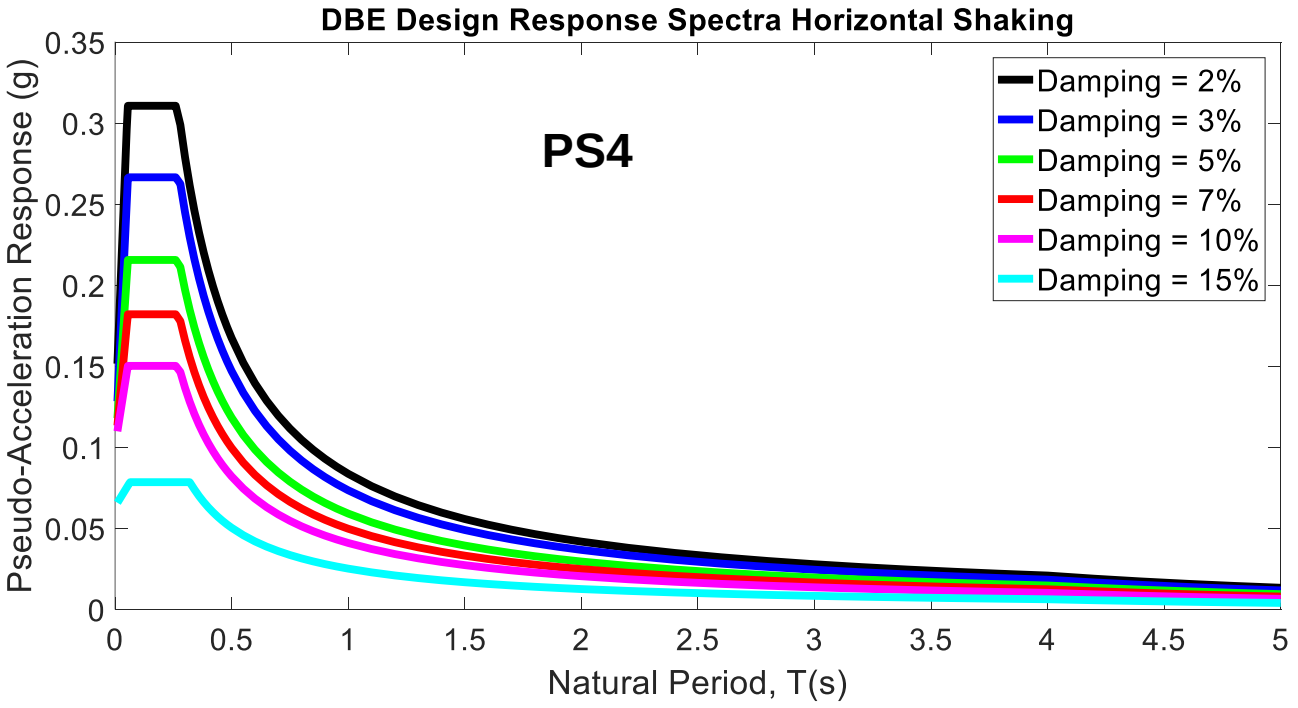

Figure 4.27: *DBE Design Response Spectra* for *Horizontal* shaking at PS4

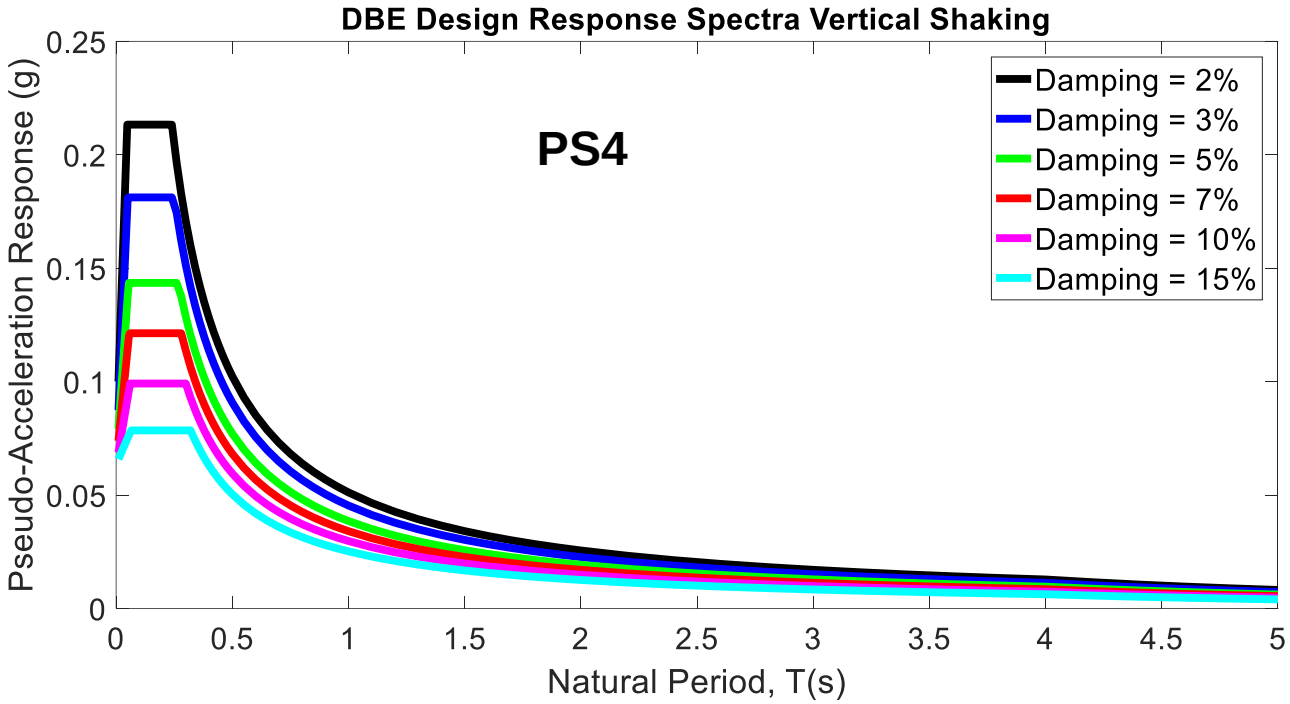

Figure 4.28: *DBE Design Response Spectra* for *Vertical* shaking at PS4

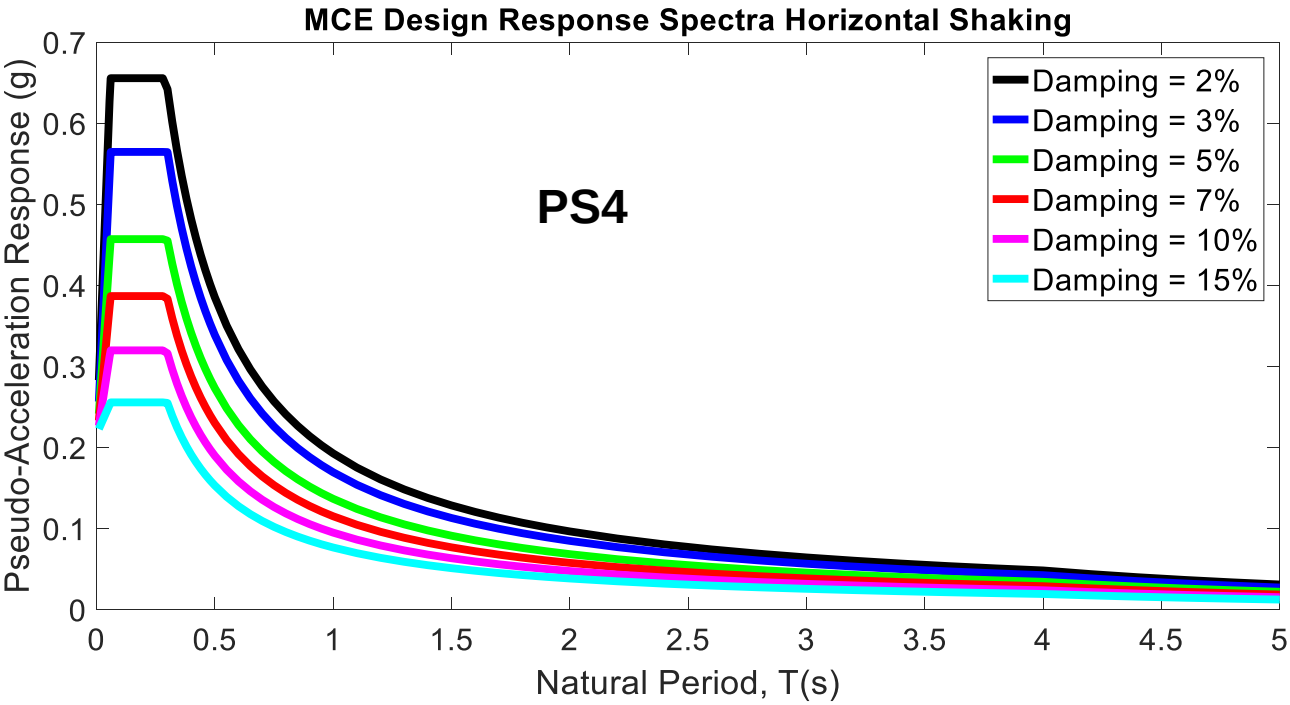

Figure 4.29: *MCE Design Response Spectra* for *Horizontal* shaking at PS4

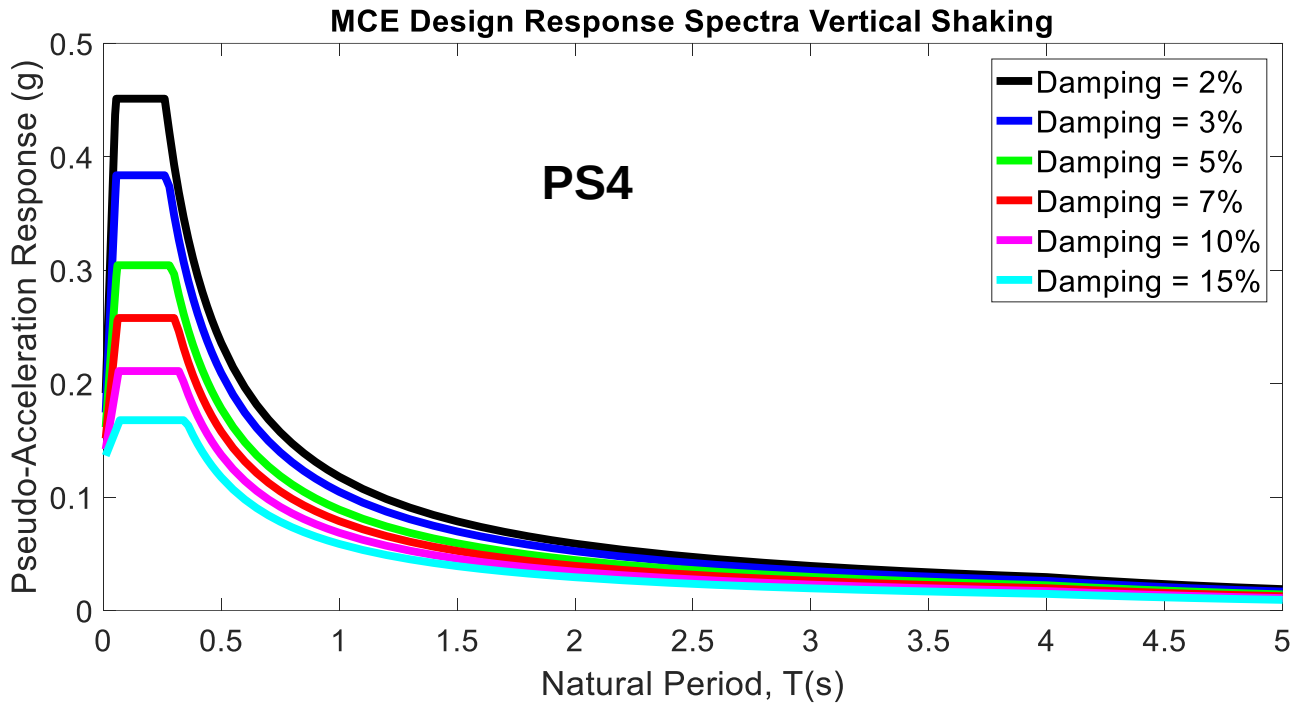

Figure 4.30: *MCE Design Response Spectra* for *Vertical* shaking at PS4

4.6 CONCLUSIONS

The following conclusions are drawn from the results of *Seismic Hazard Analysis* using the *DSHA* and *PSHA* approach:

1) The target envelope spectrum developed using the envelope of *PSHA* and *DSHA* should be used in the design of the dam site.

2) Site-specific design accelerograms and response spectra for damping values of 2%, 3%, 5%, 7%, 10% and 15 % of the horizontal and vertical ground motions for MCE and DBE conditions have been obtained for all the four locations of the dam site.

3) MCE and DBE conditions should separately be used for the specific design needs of the project.

REFERENCES

Abrahamson, N.A. and W.J. Silva (2008). Summary of Abraham and Silva NGA ground-motion relations, Earthquake Spectra, 24(1), 67-97.

Abrahamson, N. A., Silva, W. J., & Kamai, R. (2014). Summary of the ASK14 ground motion relation for active crustal regions. Earthquake Spectra, 30(3), 1025–1055. https://doi.org/10.1193/070913eqs198m

Antolik, M. and Dreger, D.S., 2003. Rupture process of the 26 January 2001 M w 7.6 Bhuj, India, earthquake from teleseismic broadband data. Bulletin of the Seismological Society of America, 93(3), pp.1235-1248.

Biswas, S. K. (1987). Regional tectonic framework, structure and evolution of the western margin basins of India. Tectonophysics, 135(4), 307–327. https://doi.org/10.1016/0040-1951(87)90115-6

Biswas, S. K. (2005). A review of structure and tectonics of Kutch basin, western India, with special reference to earthquakes. Current Science, 88, 1592–1600.

Biswas, S. K., & Khattri, K. N. (2002). A geological study of earthquakes in Kutch, Gujarat, India. Journal of The Geological Society of India, 60, 131–142.

Bollinger, G. A., Sibol, M. S., & Chapman, M. C. (1992). Maximum magnitude estimation for an intraplate setting - example: The Giles County, Virginia, Seismic Zone. Seismological Research Letters, 63(2), 139–152. https://doi.org/10.1785/gssrl.63.2.139

Boore, D.M. and J.J. Bommer (2005). Processing strong motion accelerograms: needs, options and consequences, Soil Dyn. and Earthq. Eng., 25, 93-115.

Boore, D. M., Stewart, J. P., Seyhan, E., Atkinson, G. M. (2014). NGA-WEST2 equations for predicting PGA, PGV, and 5% damped PSA for shallow crustal earthquakes. Earthquake Spectra, 30(3), 1057–1085. https://doi.org/10.1193/070113eqs184m

Bullen, K.E., (1963). An introduction to the theory of seismology: Cambridge Univ. Press.

Cornell, C.A. 1968. Engineering Seismic Risk Analysis, Bulletin of Seismological Society of America, 58, 5, 1583- 1606.

Chandra, U., 1977. Earthquakes of peninsular India—a seismotectonic study. Bulletin of the seismological Society of America, 67(5), pp.1387-1413.

Choudhury, P., Chopra, S., Kamra, C. and Das, A., 2019. New Insight into the Recent Earthquake Activity in North Cambay Basin, Western India: Seismological and Geodetic Perspectives. Bulletin of the Seismological Society of America, 109(6), pp.2240-2251.

Chung, W.Y. and Gao, H., 1995. Source mechanism of the Anjar, India, earthquake of 21 July, 1956 and its seismotectonic implications for the Kutch rift basin. Tectonophysics, 242, pp.281-292.

Chung, W.Y., 1993. Source parameters of two rift-associated intraplate earthquakes in peninsular India: the Bhadrachalam earthquake of April 13, 1969 and the Broach earthquake of March 23, 1970. Tectonophysics, 225(3), pp.219-230.

Dargahi-Noubary G.R. (1983) A procedure for estimation of the upper bound for earthquake magnitudes. Phys. Earth Planet Interiors. 33, 91-93.

Dobry, R., Borchedt, R.D., Crouse, C.B., Idriss, I.M., Joyner, W.B., Martin, G.R., Power, M.S., Rinne and Seed, R.B., (2000). New site coefficients and site 120 classification system used in recent building seismic code provisions, Earthquake Spectra, 16, No. 1, pp. 41-67, February

Foti, S., Butcher, A.P., (2004). Geophysical methods applied to geotechnical engineering. Proc. ISC-2 on Geotechnical and Geophysical Site Characterization, Viana da Fonseca & Mayne (eds.), Mill press, Rotterdam, 409- 418.

Gardner, J. K.; L. Knopoff (1974) Is the sequence of earthquakes in Southern California, with aftershocks removed, Poissonian? Bulletin of the Seismological Society of America 64 (5): 1363–1367, 10.1785/BSSA0640051363

GCMT-Global Centroid Moment Tensor Catalog (https://www.globalcmt.org/CMTsearch.html).

Gupta, I.D. (2009). Seismic hazard mapping methodologies, Int. Conf. on Earthq. Eng., Banja Luka, 26-28 October 2009, 55-101.

Gupta, I.D. (2013). Source-to-site distance distribution for area type of seismic sources used in PSHA applications, Nat. Hazards, 66, 485–499. DOI 10.1007/s11069-012-0498-5.

Gupta, I.D. and R.G. Joshi (1993). On synthesizing response spectrum compatible accelerograms, Jour. of European Earthquake Engineering, 2, 25-33.

Gutenberg, B. and C.F. Richter (1956). Earthquake magnitude, intensity, energy and acceleration, Bull. Seism. Soc. Am., 46, 105-145.

https://esdynamics.geo.uni-uebingen.de/wiki/files/remote_sensing/pdf/IPTA_users_guide.pdf

Hanks, T.H. and H. Kanamori (1979). A moment magnitude scale, J. Geophys. Res., 84, 2348-2350.

Kamra, C., Chopra, S. and Yadav, R.B.S., 2021. Joint inversion for stress and fault orientations using focal mechanisms of earthquakes in the Saurashtra horst, a part of stable continental region of India, and source parameter estimation. Journal of Seismology, pp.1-19.

Kamra, C., Chopra, S., Yadav, R.B.S. and Joshi, V., 2020. Characterization of major fault systems in the Kachchh Intraplate Region, Gujarat, India, by focal mechanism and source parameters. Seismological Society of America, 91(6), pp.3496-3517.

Kanli, A.I, Tildy, P., Pronay, Z., Pinar and Hemann, L., (2006). VS 30 mapping and soil classification for site effect evaluation in Dinar region, SW Turkey, Geophysics J.Int, Vol. 165, pp 223-235.

Kijiko A., Estimation of the Maximum Earthquake Magnitude, Mmax, Pure and Applied Geophysics, 161 (2004), pp.1–27.

Kreemer, C., Blewitt, G., & Klein, E. C. (2014). A geodetic plate motion and global strain rate model. Geochemistry, Geophysics, Geosystems, 15(10), 3849–3889. https://doi.org/10.1002/2014gc005407

Mandal, B., Vaidya, V. R., Sen, M. K., Periyasamy, K., & Sarkar, D. (2018). Common reflection surface stack imaging of the Proterozoic Chambal Valley Vindhyan basin and its boundary fault in the northwest India: Constraints on crustal evolution and basin formation. Tectonics, 37, 1393–1410. https://doi.org/10.1029/2017TC004895

McGuire, R.K. 1976. Fortran program for seismic risk analysis, U.S. Geological Survey, Open-File Report 76–67.

McGuire, R. 2004. Seismic Hazard and Risk Analysis, Earthquake Engineering Research Institute: Oakland, CA, MNO-10.

Makropoulos, K. C., & Burton, P. W. (1983). Seismic risk of circum-Pacific Earthquakes I. Strain Energy Release. Pure and Applied Geophysics PAGEOPH, 121(2), 247–267. https://doi.org/10.1007/bf02590137

NCSDP (2011, Revised 2014). Guidelines for Preparation and Submission of Site-Specific Seismic Study Report of River Valley Project to National Committee on Seismic Design Parameters, National Committee on Seismic Design Parameters, FE&SA Directorate, Central Water Commission, New Delhi.

Nagabhushana Rao, Ch., N. Purnachandra Rao, B.K. Rastogi (2013) Evidence for right-lateral strike-slip environment in the Kutch basin of northwestern India from moment tensor inversion studies, Journal of Asian Earth Sciences 64, 158–167.

Novikova, E.I. and Trifunac.M.D. (1994). Duration of strong ground motion. Scaling in terms of earthquake magnitude, epicentral distance and geological and local soil conditions, Earthq. Eng. And Struct. Dyn., 23(6), 1023-1043

Rajewar, SK, Ch. Mohana Lakshmi, Aditya Mohanty, Dwijendra N. Pandey, Anshuman Pandey, Anurag Chaurasia, Ananya Pandey, V. Rajeswar Rao, M.S. Naidu, Amit Kumar, Saroj K Mondal, Rajeev K Yadav, J.K. Catherine, R.K. Giri,

V.K. Gahalaut (2021) Constraining Plate Motion and Crustal Deformation from GNSS Measurements: CSIR-NGRI Contribution, Journal Geological Society of India, 97, 10.1007/s12594-021-xxxx-x.

Rao, C.N., Rao, N.P. and Rastogi, B.K., 2013. Evidence for right-lateral strike-slip environment in the Kutch basin of northwestern India from moment tensor inversion studies. Journal of Asian Earth Sciences, 64, pp.158-167.

Roy, A. B. (2004). The Phanerozoic reconstitution of Indian shield as the aftermath of break-up of the Gondwana land. Gondwana Research, 7(2), 387–406. https://doi.org/10.1016/S1342-937X(05)70792-9

Stepp, J.C. (1973). Analysis of completeness of the earthquake sample in the Puget sound area, in `Seismic Zoning (edited by S.T. Harding),' NOAA Tech. Report ERL 267-ESL30, Boulder, Colorado, USA.

Uhrhammer, R.A. (1986). Characteristics of northern and central California seismicity; Earthquake Notes, 57(1), 21 (abstract)

Vijaya Rao, V., Rajendra Prasad, B., Reddy, P. R., & Tewari, H. C. (2000). Evolution of Proterozoic Aravalli Delhi fold belt in the northwestern Indian shield from seismic studies. Tectonophysics, 327(1-2), 109–130. https://doi.org/10.1016/S0040-1951(00)00156-6

Vijaya Rao, V., Reddy, P.R., 2002. A Mesoproterozoic supercontinent: evidence from the Indian Shield. In: Rogers, J.J.W., Santosh, D.M. (Eds.), Special volume on Mesoproterozoic Supercontinent, Gondwana Research 5, 63–74.

Wegnüller, Charles Werner, Tazio Strozzi, Andreas Wiesmann, Othmar Frey, Maurizio Santoro, "Sentinel-1 Support in the GAMMA Software, Procedia Computer Science, Volume 100, 2016, Pages 1305-1312, ISSN 1877-0509, https://doi.org/10.1016/j.procs.2016.09.246.

Wegmüller, C. Werner, T. Strozzi and A. Wiesmann "Multi-Temporal Interferometric Point Target Analysis" (2004), 10.1142/9789812702630_0015

Weichert, D.H. (1980). Estimation of the earthquake recurrence parameters for unequal observation periods for different magnitudes, Bull. Seism. Soc. Am., 70(4), 1337-1346.

Wells, D.L. & Coppersmith K.J. (1994) New Empirical Relationships among Magnitude, Rupture Length, Rupture width, Rupture Area, and Surface Displacement. Bulletin of the Seismological Society of America, 84, 974-1002.

Wheeler, R. L. (2009). Methods of Mmax estimation east of the Rocky Mountains. Open-File Report. https://doi.org/10.3133/ofr20091018

Contributors

Ayushi Tiwari
I D Gupta
M Ravikumar
Shiv More
Rajeev Kumar Yadav
D Srinagesh
Vineet K Gahalaut

CSIR-National Geophysical Research Institute, Uppal Road, Hyderabad 500007